

Los Alamos National Laboratory is operated by the University of California for the United States Department of Energy under contract W-7405-ENG-36.

DO NOT CIRCULATE

PERMANENT RETENTION

REQUIRED BY CONTRACT

*Hypervelocity Impact Studies on
Titanium, Titanium Alloys,
and Beryllium*

LOS ALAMOS NATIONAL LABORATORY



3 9338 00308 6344

Los Alamos Los Alamos National Laboratory
Los Alamos, New Mexico 87545

This work was supported by the US Department of Energy, Office of Coordination and Special Projects.

DISCLAIMER

This report was prepared as an account of work sponsored by an agency of the United States Government. Neither the United States Government nor any agency thereof, nor any of their employees, makes any warranty, express or implied, or assumes any legal liability or responsibility for the accuracy, completeness, or usefulness of any information, apparatus, product, or process disclosed, or represents that its use would not infringe privately owned rights. References herein to any specific commercial product, process, or service by trade name, trademark, manufacturer, or otherwise, does not necessarily constitute or imply its endorsement, recommendation, or favoring by the United States Government or any agency thereof. The views and opinions of authors expressed herein do not necessarily state or reflect those of the United States Government or any agency thereof.

LA-9417-MS

UC-25

Issued: August 1982

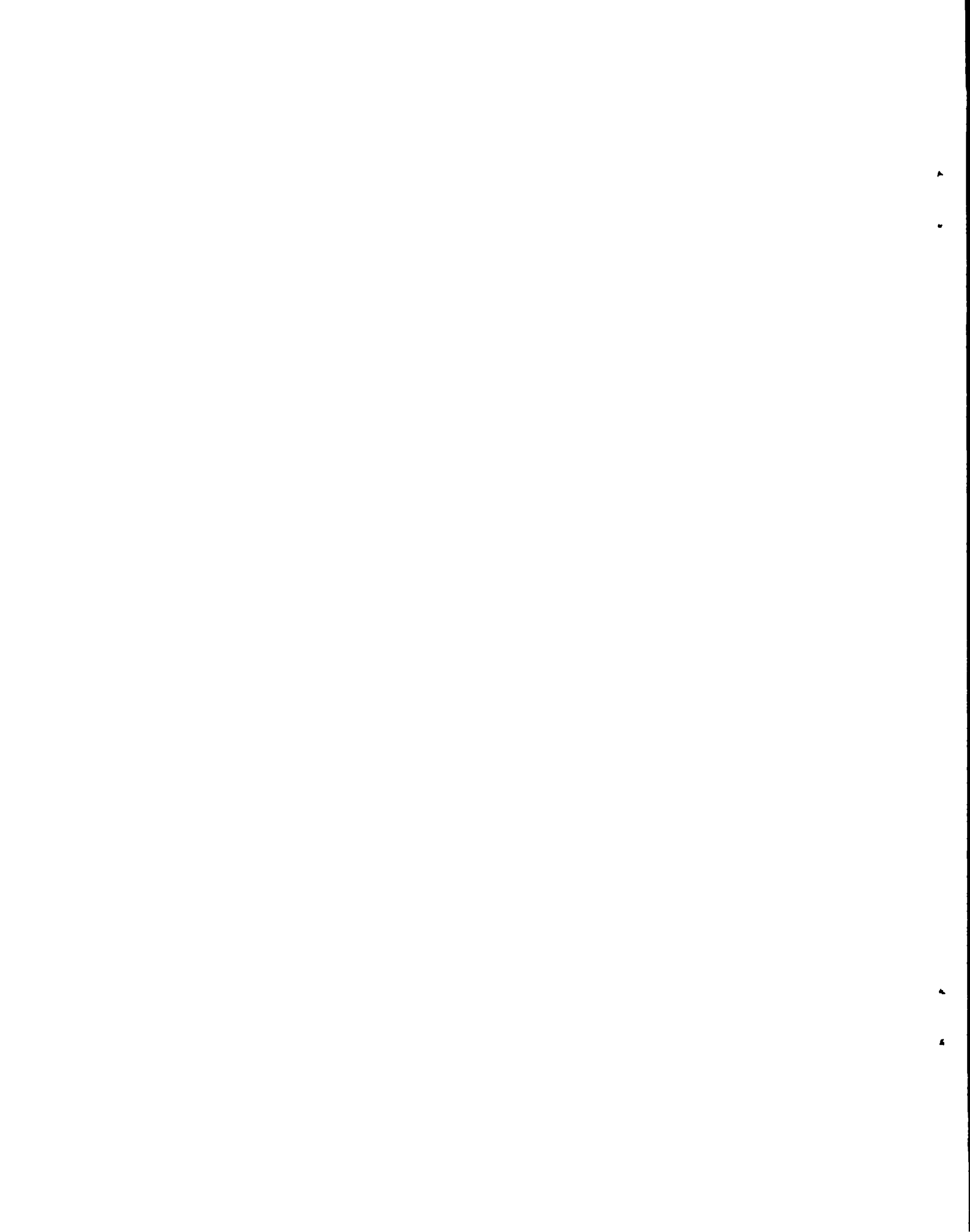
Hypervelocity Impact Studies on Titanium, Titanium Alloys, and Beryllium

L. B. Lundberg
S. J. Bless*
S. P. Girrens
J. E. Green*



* Department of Physics, University of Dayton Research Institute, Dayton, OH 45469.

Los Alamos Los Alamos National Laboratory
Los Alamos, New Mexico 87545



CONTENTS

ABSTRACT.	1
I. INTRODUCTION	1
II. BACKGROUND	2
A. Radiator Heat Pipe Failure.	2
B. Meteoroid Threat.	3
C. Hypervelocity Impact Behavior Extrapolation	6
D. Previous Experimental Work.	7
III. EXPERIMENTAL APPROACH.	8
A. Range Description	9
B. Target Materials.	24
IV. EXPERIMENTAL RESULTS	28
A. Thick Targets	29
B. Thin Targets.	39
V. DATA ANALYSIS.	50
A. Thick Targets	50
B. Threshold Penetration vs Crater Depth for Titanium.	55
VI. DISCUSSION	56
A. Material Behavior	56
B. Implications for Radiator Design.	58
VII. CONCLUSIONS AND RECOMMENDATIONS.	60
ACKNOWLEDGEMENTS.	61
REFERENCES.	61

FIGURES

1. Space reactor power system with multiple heat pipe radiator. . . .	3
2. Defocusing factor due to Earth's gravity for average meteoroid velocity of 20 km/s.	5
3. Method for determining body shielding factor for randomly oriented spacecraft.	5
4. University of Dayton Range Configuration for the "Meteoroid" Program.	9
5. Light-gas gun operational sequence	10

6.	Light-gas gun.	11
7.	Schematic of basic light-gas gun with gas seals and burst-diaphragm locations.	13
8.	Burst-diaphragm, die, and seal disc.	14
9.	Burst-diaphragm and seal after a shot.	14
10.	Left: Serrated sabot with 1.4-mm glass bead in pocket. Right: Expected in-flight attitude	15
11.	Sabot-stripper with shorting pin	16
12.	Radiograph of sabot opening in flight.	17
13.	Target heating apparatus with target in position for impacting . .	18
14.	Target chamber used for beryllium targets.	20
15.	Diagram of range instrumentation employed in initial technique-development shots.	20
16.	Framing camera record from Shot 96	21
17.	Enlargement of frames 21-44 from Fig. 16	22
18.	Sabot plates and target from Shot No. 78	23
19.	Portion of record showing typical cut-off of second laser beam by projectile and other material launched by gun. The passage of the projectile can be identified as the short downward spike. Data from Shot No. 84.	23
20.	Typical record of muzzle flash from light-gas gun. Data from Shot No. 79.	24
21.	Volumes of craters made in steel sabot plates by 0.15-g sabot segments. Open circles were RC 20 hardness, closed circles were RC 30	25
22.	Preshot microstructure of Grade 2 titanium bar used in impact tests, longitudinal section.	26
23.	Preshot microstructures of (a) Ti-5Al-2.5Sn and (b) Ti-6242 Si used in impact studies, longitudinal sections.	27
24.	Preshot microstructure of beryllium used in impact tests, longitudinal section	29
25.	Titanium bar impacted at room temperature with a glass bead (Shot No. 84): (a) crater cross section, (b) crater bottom, and (c) right side of crater	31

26.	Titanium bar impacted at room temperature with a copper sphere (Shot No. 89): (a) crater cross section, (b) crater bottom, and (c) right side of crater	32
27.	Titanium plate impacted at 775 K with an aluminum sphere (Shot 134): (a) crater cross section, (b) left side of crater, (c) crater bottom, (d) halfway between crater bottom and incipient spall, and (e) incipient spall zone.	33
28.	Titanium plate impacted at 775 K with a cadmium sphere (Shot No. 147): (a) crater cross section, (b) crater bottom, and (c) left side of crater.	34
29.	Titanium plate impacted at 775 K with a copper sphere (Shot No. 133)	36
30.	Copper-projectile-produced craters in: (a) Ti-6242Si, (b) Grade 2 Ti (Shot No. 131), and (c) Ti-5Al-2.5Sn targets maintained at 775 K.	37
31.	Ti-5Al-2.5Sn alloy impacted at 775 K with a copper sphere (Shot 151): (a) impact crater cross section, (b) crater lip, (c) crater bottom, and (d) crater side wall.	38
32.	Hypervelocity impact crater in Ti-5Al-2.5Sn, impacted with a copper sphere at 775 K	39
33.	Ti-6242 Si alloy impacted at 775 K with a copper sphere (Shot 150): (a) optical micrograph of crater, (b) SEM of crater bottom, (c) SEM, (d) optical micrograph of crater side wall, and (e) SEM of crater bottom surface.	40
34.	Beryllium target impacted with a copper sphere at room temperature (Shot No. 159)	41
35.	Beryllium impacted with a copper sphere at room temperature (Shot No. 159): (a) crater cross section, (b) SEM, and (c) optical micrographs of crater bottom	42
36.	Photograph sequence made with the B&W 300 high-speed camera, from Shot No. 95: (a) 1-mm-glass bead in flight at 6.12 km/s, (b) bead has impacted on 2.78-mm-thick Grade 2 Ti target, and (c) spall break-out of back side of target	43
37.	Rear surface from Shot No. 95, showing where spall was ejected.	44
38.	Titanium plate impacted at 775 K with a copper sphere (Shot No. 141): (a) impact crater on front surface and (b) bulged and spalled rear surface	45

39.	Titanium plate impacted at 775 K with a glass bead (Shot No. 137): (a) impact crater on front side, (b) bulged and spalled rear surface, and (c) crater cross section	46
40.	Titanium plate impacted at 775 K with a glass sphere (Shot No. 143) at 45°: (a) perforated crater, (b) crater bottom, and (c) crater side.	48
41.	Photomicrograph of target from Shot No. 158: 0.66-mm-thick, shot-peened titanium plate struck by 0.5-mm bead	49
42.	Crater volume data for thick titanium targets fitted to $V = E/\epsilon$	52
43.	Crater depth data for thick titanium targets fitted to C-S equation.	53
44.	Dependence of C-S penetration parameter on projectile density for titanium. Open circles, 775 K targets; closed circles, 295 K	53
45.	Dependence of cratering coefficient on projectile density for titanium. Open circles, 775 K targets; closed circles 295 K	54
46.	Radiator mass vs meteoroid mass for armor thicknesses calculated with the C-S equation.	59

TABLES

I.	CHEMICAL ANALYSIS OF TARGET MATERIALS	26
II.	IMPACT DATA	30
III.	SHOT-BLASTED AND COATED TARGET DATA	49
IV.	SUMMARY OF THICK-TARGET CRATER DATA	51
V.	THIN-TARGET RESULTS OBTAINED IN THIS STUDY FOR GRADE 2 Ti at 775 K	55
VI.	THIN-TARGET OBLIQUE IMPACT RESULTS OBTAINED BY BRUCE ⁹ FOR GRADE 4 Ti AT ROOM TEMPERATURE.	56
VII.	RADIATOR DESIGN CRITERIA.	58

HYPERVELOCITY IMPACT STUDIES ON TITANIUM, TITANIUM ALLOYS, AND BERYLLIUM

by

L. B. Lundberg, S. J. Bless,
S. P. Girrens, and J. E. Green

ABSTRACT

The hypervelocity impact behavior of commercial-pure, Grade 2 Ti, Ti-5Al-2.5Sn, Ti-6Al-2Sn-4Zr-2Mo-0.25Si, and pure beryllium was studied by impacting targets of these materials with millimeter-sized spheres of glass, copper, aluminum, and cadmium propelled from a light-gas gun at velocities ranging from 4.5 to 7.6 km/s. Target temperatures ranged from 295-775 K when impacted. Semi-infinite targets were impacted to determine cratering behavior, and some correlations were made to thin-target perforation. Thin titanium targets with a variety of surface coatings and finishes were also impacted. Titanium and the titanium alloys were found to behave in a ductile manner when impacted, but beryllium was found to be brittle even at 775 K. An extrapolation equation was used to optimize a titanium heat pipe radiator mass for a space nuclear power application.

I. INTRODUCTION

Even early science fiction writers recognized that meteoroid impact was an extraterrestrial environmental hazard. As space vehicles were developed, a concerted effort was made to determine incident meteoroid fluxes and to devise practical countermeasures. Almost a decade ago, successful meteoroid bumper technology was developed. Bumpers consisting of thin metal plates standing off from the structural surface have been adequate for protecting spacecraft hulls, and there has been little research in meteoroid-impact phenomena since.

Presently, we are entering a new stage in space technology. Serious planning is underway for placing complex structures and facilities into orbit. These activities have resurrected the need for scientific and engineering study of hypervelocity impact phenomena.

Experimental work was performed in support of the nuclear electric power plant described by Ranken and Koenig.¹ The system design features a large radiator like that shown in Fig. 1, composed of arrays of heat pipes to dispose of the waste heat from thermoelectric converter devices. The design specification calls for the probability of the radiator not being able to reject the specified amount of heat to be less than 1% over a 7-yr period. One failure mechanism is loss of heat pipe fluid from heat pipes that are perforated by micrometeoroids. The objective of the experimental effort described below was to acquire data to support the analysis of this problem.

Unfortunately, a space radiator cannot be protected by a simple bumper system and still radiate efficiently. Various designs have been proposed for the radiator structure. All involve tradeoffs between probability of loss of any individual heat pipe and the redundancy in number of heat pipes. Only experimental data for meteoroid perforation resistance of candidate materials can allow the minimum weight radiator to be designed.

Early calculations for the design of radiators operating above 650 K indicated minimum weights might be obtained if the heat pipes were constructed from beryllium or Ti-6Al-4V and the working fluid was potassium.² Because the literature contained insufficient data on the hypervelocity impact behavior of these or similar materials, the University of Dayton Research Institute (UDRI) was engaged to perform an experimental study of the hypervelocity impact behavior of beryllium, titanium, and two titanium alloys, Ti-5Al-2.5Sn and Ti-6Al-2Sn-4Zr-2Mo, at room temperature and 775 K. This study and its consequences toward radiator design are described below.

II. BACKGROUND

A. Radiator Heat Pipe Failure

Radiator heat pipes are evacuated metal containers that contain a working fluid that circulates between heated (evaporator) and cooled (condenser) regions. Heat is absorbed by the working fluid, causing it to vaporize, and the

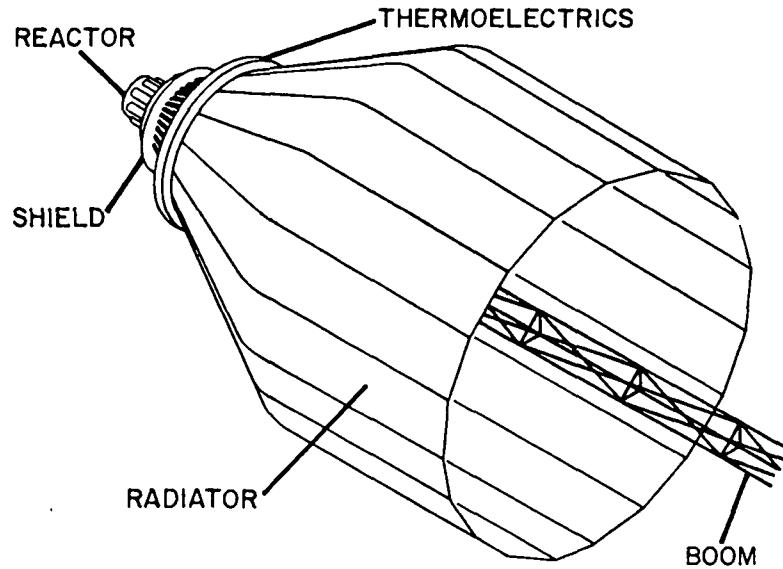


Fig. 1. Space reactor power system with multiple heat pipe radiator.

vapor flows to the condenser where the absorbed heat is released as the fluid condenses. The liquid working fluid is then pumped back to the evaporator through a screen wick or other porous medium by capillary action. In a properly designed heat pipe, both the evaporation and condensation take place at approximately the same temperature, so that heat is transferred between two reservoirs nearly isothermally.

Because a radiator heat pipe must be directly exposed to space, it is not practical to protect it from meteoroid penetration with a shield or bumper. A puncture in an operating heat pipe container results in rapid loss of the vaporizing working fluid to space. Meteoroid impacts which cause the heat pipe container wall to either dimple or spall without puncturing are not expected to adversely affect heat pipe operation. Therefore, when armoring the surfaces of a radiator heat pipe exposed to space, concern is directed towards determining the threshold penetration thickness (TPT) of the container material that is required to prevent penetration by a meteoroid with specified mass and velocity.

B. Meteoroid Threat

In order to begin the solution of the radiator design problem, it is first necessary to quantify the number, mass, and velocity of meteoroids that can potentially collide with it. Because meteoroids are solid particles moving in

interplanetary space, they can be quantified with average density, velocity, and mass-flux models. The Near Earth to Lunar Surface Meteoroid Environment Model³ published by the National Aeronautics and Space Administration (NASA) was selected for use in the preliminary design of the Space Power Advanced Reactor (SPAR) system. The near-Earth average total meteoroid (average sporadic plus average stream) mass-flux model is

$$\text{for } 10^{-6} \leq m < 1, \log_{10} N_t = -14.37 - 1.213 \log_{10} m \quad , \quad (1)$$

where

$$\begin{aligned} N_t &= \text{number of particles of mass } m \text{ or greater/m}^2 \cdot \text{s} \\ m &= \text{particle mass (g)}. \end{aligned}$$

The average particle density and velocity associated with this mass-flux model are 0.5 Mg/m^3 and 20 km/s , respectively. Particles with these properties will be termed "standard meteoroids" in this report. To correct for the Earth's gravitational effect at a given distance above the Earth, N_t must be multiplied by the defocusing factor, G_e , which is obtained from Fig. 2. To correct for planetary body shielding, the unshielded defocused flux is multiplied by the shielding factor, e . The shielding factor is determined as described in Fig. 3.

With the previously described mass-flux model and the Poisson distribution equation

$$P_{x \leq n} = \sum_{r=0}^{r=n} \left[\frac{e^{-N_t A \tau} (N_t A \tau)^r}{r!} \right] \quad (2)$$

where $P_{x \leq n}$ = probability of impact by n meteoroids or less,
 N_t = expected flux (particles/ $\text{m}^2 \cdot \text{s}$),
 A = exposed area (m^2), and
 τ = exposure time (s),

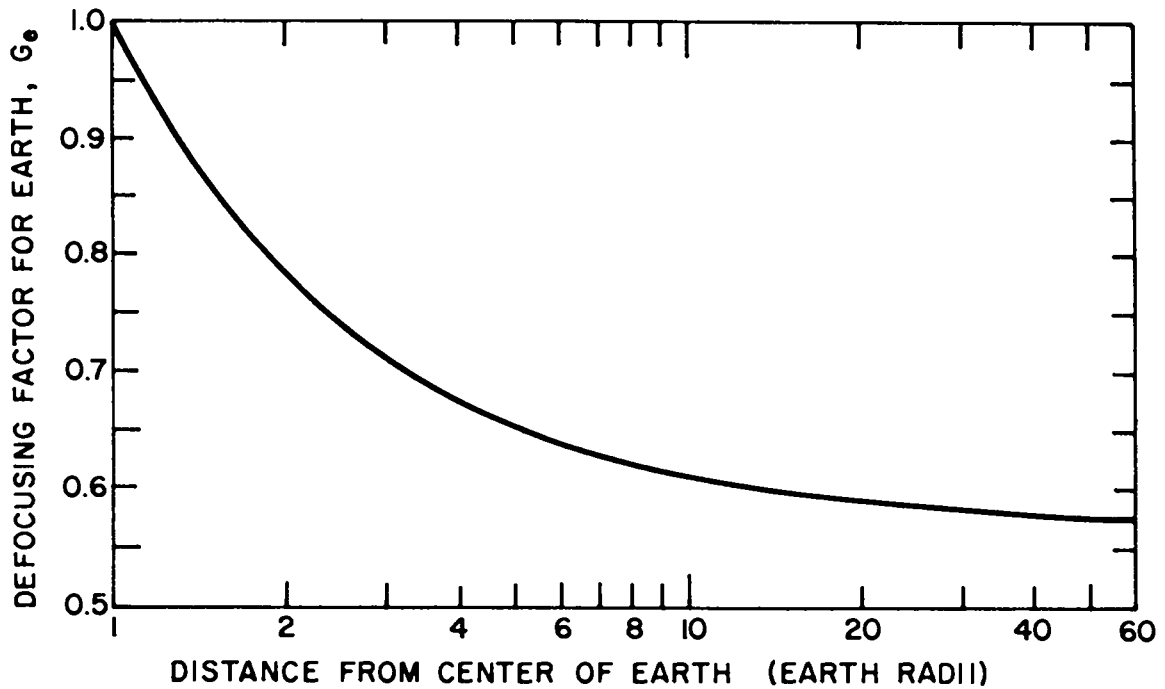


Fig. 2. Defocusing factor due to Earth's gravity for average meteoroid velocity of 20 km/s.

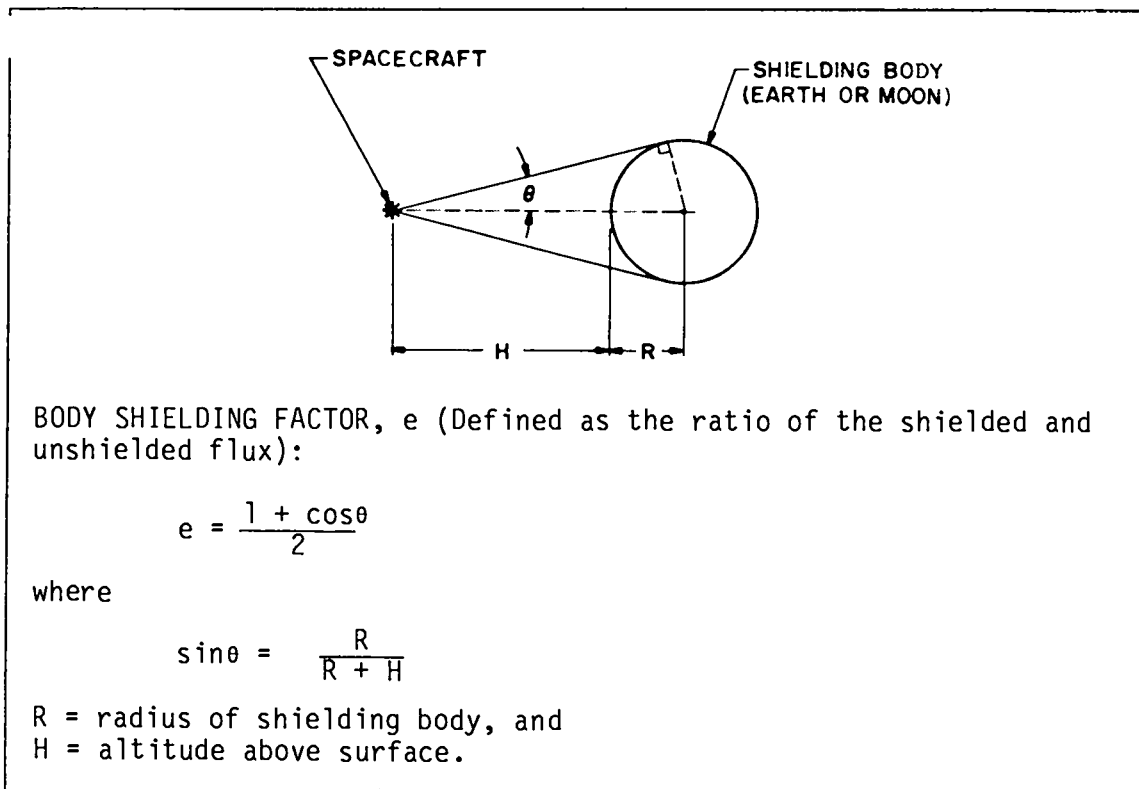


Fig. 3. Method for determining body shielding factor for randomly oriented spacecraft.

the probability of impact by n particles of mass m or greater can be established. Thus, by armoring the heat pipes to withstand impacts from a specified mass of meteoroid, the number of impacts from larger particles can be predicted and the probability of heat pipes being penetrated determined. The specification of the armor thickness depends on the hypervelocity impact resistance of the armor material.

C. Hypervelocity Impact Behavior Extrapolation

Because the "average" near-Earth meteoroids have not been reliably simulated in the laboratory, it is necessary to extrapolate hypervelocity impact data obtained at lower velocities and higher projectile densities. Many empirical formulas have been proposed for extrapolating hypervelocity cratering and perforation data (for full discussions of the several formulas see Refs. 4 and 5).

The hypervelocity penetration equation developed for normal impact of semi-infinite targets by Charters and Summers, and recommended by Schneider,⁶ is:

$$p/d = 1.5 \left(\frac{\rho_p}{\rho_t} \right)^{1/3} \left(\frac{\rho_p u^2}{2 S_t} \right)^{1/3}, \quad (3)$$

where p = crater depth;
 d = projectile diameter;
 ρ_p = mass density of projectile;
 ρ_t = mass density of target;
 u = projectile velocity; and
 S_t = material constant.

After Schneider,⁶ we refer to this as the C-S equation. It should be pointed out that this equation assumes a hemispherical crater. The parameter S_t is an empirical quantity depending on target material properties. We have found it convenient to rewrite Eq. (3) as

$$p = \left(\frac{81}{4\pi} \frac{\rho_p}{\rho_t} \frac{E}{S_t} \right)^{1/3}, \quad (4)$$

where E is the kinetic energy of a spherical projectile. In this formulation, it can be readily seen that p is inversely proportional to $S_t^{1/3}$, which has the units $(\text{energy/volume})^{1/3}$. In this report, $S_t^{1/3}$ is expressed in $(\text{GJ/m}^3)^{1/3}$. Equation (3), and consequently, Eq. (4) were derived from tests performed at velocities below the speed of sound in the target, and according to Gehring,⁴ these equations overpredict the effect of particle density on both penetration and crater volume. Nevertheless, the data derived from this study are analyzed using these equations.

Schneider⁶ also indicates that in the hydrodynamic (hypervelocity) regime the crater volume is proportional to the kinetic energy of the impact particle. Thus, the crater volume can be written in terms of a cratering efficiency parameter, ϵ , as

$$V = E/\epsilon \quad (5)$$

The parameter ϵ has dimensions GJ/m^3 and can be compared to the parameter S_t of Eq. (4).

Experience in ballistics and hypervelocity impact indicates that the crater depth in a semi-infinite plate is proportional to the thickness of a plate that can be impacted under the same conditions and just perforated. This condition for the finite plate is commonly referred to as the threshold penetration thickness (TPT), and its value is commonly approximated to be 1.5 times the semi-infinite plate crater depth. Experimental studies have indicated that the proportionality constant, K_0 , can be as high as 2.0 (Ref. 7). We consider K_0 to be a parameter in this study and write

$$\text{TPT} = K_0 p. \quad (6)$$

D. Previous Experimental Work

There have been very few previous studies relevant to hypervelocity cratering in titanium, titanium alloys, and beryllium. The information that the authors could locate is summarized below.

Diedrich, et al.⁸ conducted a study for a reactor radiator that included four shots into thick hot-pressed beryllium. The temperature was 975 K, the projectiles were $\rho = 2.51 \text{ Mg/m}^3$ Pyrex, and impact velocities were 7-8 km/s. Beryllium was observed to behave in a brittle manner; there was a great deal

of front surface spall. Also, much secondary cracking of the metal extending large distances from the crater was observed. Crater depths are reported for three shots that give values of $S_t^{1/3}$ between 3.02 and 3.81 $(\text{GJ}/\text{m}^3)^{1/3}$. The mean was 3.35 $(\text{GJ}/\text{m}^3)^{1/3}$.

Gehring⁴ reports a value of $\epsilon^{1/3}$ for titanium of 1.9 $(\text{GJ}/\text{m}^3)^{1/3}$. This apparently derives from a datum reported by an author, which in turn is based on a single datum of a previous author at 2.3 km/s obtained in 1955, probably from a shaped charge jet.

Bruce^a has communicated to us some unpublished data obtained for GE at the Arnold Engineering Development Center (AEDC) during the '60s. The data are for Grade 4 commercially pure titanium (AMS 4921) impacted at room temperature. There were three normal shots into semi-infinite targets at 6.1-7.5 km/s using spherical 302 stainless steel (SS) projectiles. The resulting value of $S_t^{1/3}$ is $3.86 \pm 0.20 (\text{GJ}/\text{m}^3)^{1/3}$. Bruce had reported earlier on oblique hypervelocity impacts into titanium sheets of the same grade (AMS 4901) at room temperature.¹⁰ It was found that the thickness of the sheet parallel to the projectile's trajectory that just resisted penetration ranged from 1.74-2.09 times the crater depth in a comparable semi-infinite target.

Clough, et al.⁷ studied the hypervelocity impact behavior of Ti-6Al-4V at 699 K. Spherical Pyrex ($\rho_p = 2.26 \text{ mg}/\text{m}^3$) projectiles were impacted normal to the surface of the heated targets at velocities ranging from 7.50-7.84 km/s. A value of $(S_t)^{1/3} = 3.80 (\text{GJ}/\text{m}^3)^{1/3}$ was calculated from their penetration data for the single shot into a semi-infinite target. They also determined that $K_0 = 1.65$ for thin Ti-6Al-4V targets.

III. EXPERIMENTAL APPROACH

In order to simulate near-Earth micrometeoroid impacts into candidate radiator heat pipe armor materials, we chose to impact targets with a variety of millimeter-sized spheres propelled by a two-stage, light-gas gun to velocities in excess of the speed of sound in the target. In this system, projectiles can be well characterized in flight, and reasonable control can be maintained over the experimental conditions. Projectile masses and velocities were chosen to bracket the kinetic energy of "average" near-Earth meteoroids, and in some cases the targets were heated to simulate the operating environment of the radiator. Most of the targets were semi-infinite, but a few thin targets were

^aThis information provided by E. Bruce, The General Electric Co.

shot to check the value of K_0 . All shots were conducted on the UDRI light-gas gun range described below.

A. Range Description

As shown schematically in Fig. 4, the range consists of a light-gas gun projectile launching unit, a blast tank, and a target tank. Instrumentation for determining projectile velocity and integrity are located at both the blast tank and the target tank. The design and operation of these components are detailed below.

1. Launch Unit.

a. Light-Gas Gun. The basic operational sequence of the light-gas gun is shown in Fig. 5. The gun consists of the following components: the breech, the pump tube, the high-pressure section, and the launch tube. The propellant chamber is a 40-mm MK4 barrel with a screw breech and is fired by an electrical solenoid that actuates the firing pin. The pump tube is 41.9 mm i.d. and is 1.52 m long. A high-pressure transition section couples the 40-mm launch tube to smaller diameter pump tubes. A 7.62-mm-i.d. pump tube was used in this program; in other programs, pump tubes up to 20 mm i.d. have been used.

Gun mounting techniques, alignment procedures, maintenance, and range evacuation systems were typical of ballistic ranges at UDRI and elsewhere, so

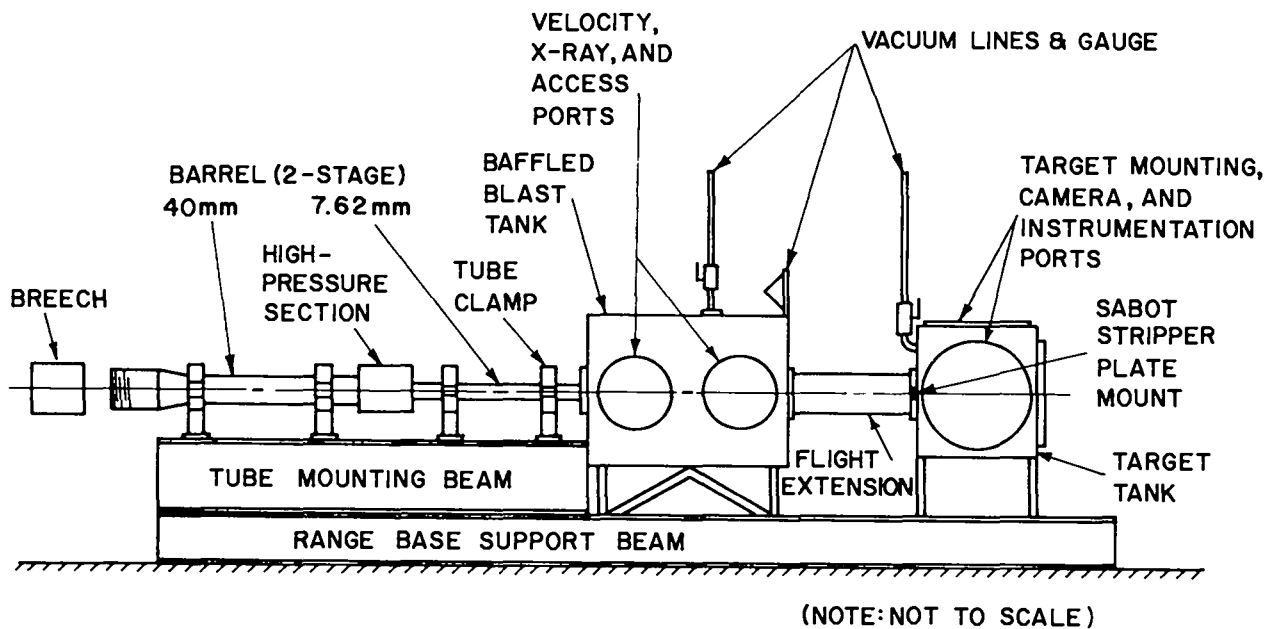


Fig. 4. University of Dayton Range Configuration for the "Meteoroid" Program.

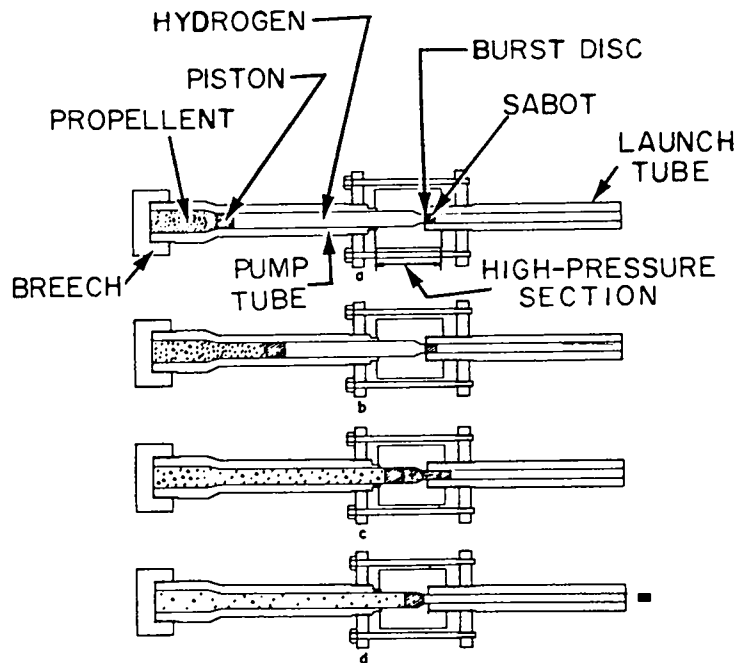


Fig. 5. Light-gas gun operational sequence. (a) Propellant in breech behind driving piston, gas (hydrogen) at rest between piston, and burst-disc in pump tube. Projectile/sabot at rest in launch tube. (b) Propellant ignited, piston moves forward compressing gas in pump tube. (c) High gas pressure ruptures burst-disc and starts projectile/sabot accelerating down launch tube. (d) Driving piston lodges into high pressure section while expanding gas in launch tube forces sabot/projectile from launch tube into a free-flight state.

will not be described in detail herein. An overall view of one configuration of the light-gas gun is shown in Fig. 6.

The light-gas gun is a subsonic piston type. It employs a reservoir of highly compressed, low-molecular-weight gas (H_2 or He) to accelerate the piston. The very high sound speed of the driving gas allows projectiles to be accelerated to velocities several times those of conventional guns. The reservoir of energetic gas is produced in the gun by compressing hydrogen in a sealed gun barrel (pump tube) with a propellant-driven piston. The gas is compressed into the high-pressure section until the pressure exceeds the resistance of a rupture diaphragm between the high-pressure section and the launch tube. The gas is then further compressed by the forward acceleration of the piston while it escapes down the launch tube behind the accelerating projectile-carrying sabot. The piston is stopped in the high-pressure section after transferring nearly all its energy to the gas. The peak pressures in the high-pressure section are in the neighborhood of 1.5 GPa. Adiabatic heating of the compressed hydrogen results in temperatures exceeding 6000 K.

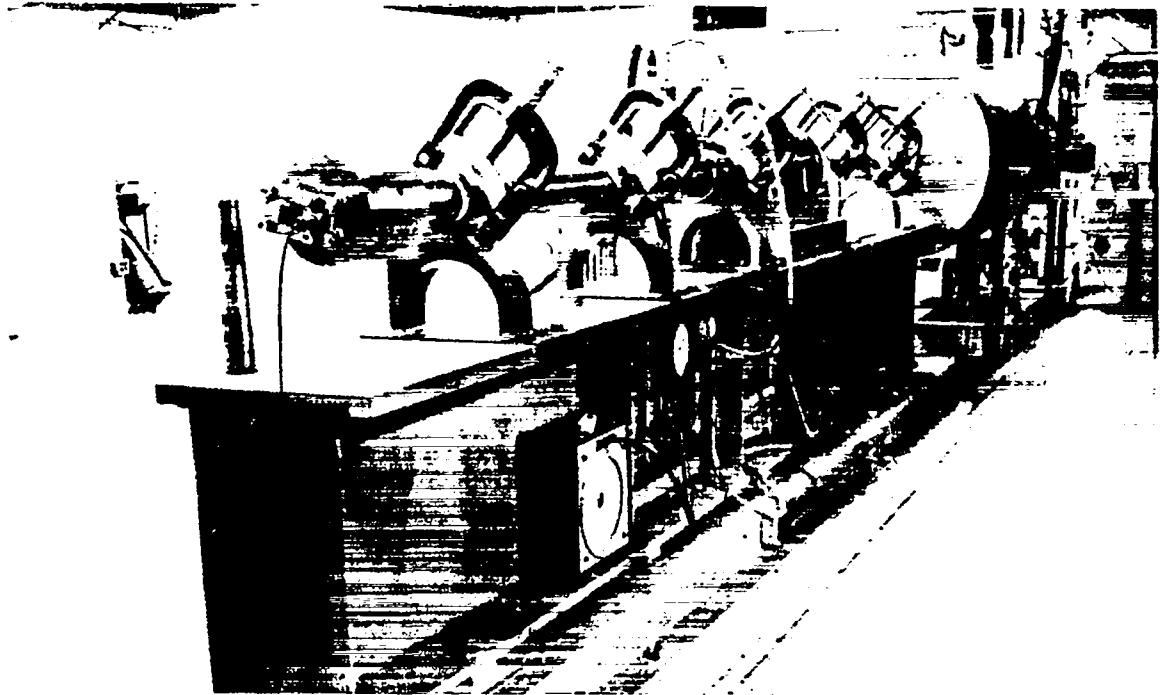


Fig. 6. Light-gas gun.

The launch barrel suffers severe erosion at its breech due to the high temperature. The only remedy for the erosion was to cut off the worn portion-- usually ~ 100 mm. This had to be done about every ten shots. Two launch tubes were used in the program in order to minimize downtime during these machining operations.

The light-gas gun has several regions that are subjected to extremely high pressures. The gun performance is limited by the material strength in these regions. The most critical regions are at the breech, the high-pressure section, and the interface between the pump and launch tubes and the high-pressure section itself.

Breech pressures decrease rapidly with forward displacement of the piston. Thus, the high-strength portion need extend only a limited distance. Stresses in the breech are held within the elastic limits of the material.

The highest gas pressures in the gun are developed in the high-pressure section. They are of such magnitude that they can be contained only through plastic deformation at the inside of the thick-walled section. The calculated gas pressures, which in the past have been the design criteria of the high-

pressure section, are not necessarily the peak pressures to be contained. Extrusion pressures created by the impact of the polyethylene piston may be considerably greater than the gas pressures.

At the high-pressure section/barrels interface, the gas pressure in the barrels must be contained with a seal arrangement that permits the high-pressure section and barrels to be easily assembled and disassembled. During the present program, the gun performance was considerably improved by modifications to the seal designs in these areas. It has been stated that there are four main variables that control the performance of the light-gas gun: the propellant mass, the piston mass, the hydrogen gas pressure, and the projectile mass. Our experience suggests a fifth variable crucial to the gun's performance--the burst-diaphragm strength.

b. Gun Development. Having established a seven/eleven powder weight ratio (grams/gas pressure, in psi) from a series of test shots and keeping the piston and projectile mass the same, efforts were focused on efficient gas seals and burst-diaphragm thicknesses for this particular gun configuration. Original burst-diaphragms and seals used in the first series of launches were made from medium to hard copper, and 2024-T3 and 6061-T6 aluminum. The diaphragms were sandwiched between the high-pressure section and launch tube, and the seals placed between the high-pressure section and pump tube. Difficulties were experienced in maintaining proper seals at both the front and rear faces of the high-pressure section. Leakage at the front face reduced the maximum gas pressure that could be built up between the piston and the burst diaphragm and gas leakage at the rear of the high-pressure section reduced the driving force of the launch sabot. Seal failures also resulted in seizure of the components due to the peripheral expansion of the various materials being used in the series of tests. This made dismantling the gun difficult and time consuming. Most important of all, it was not possible to reliably launch projectiles over 6 km/s. At higher velocities the sabots apparently broke in the barrel.

The original burst-diaphragm design was that of a shear disk. This design had been used successfully in previous programs with larger diameter launch tubes and nondiscarding sabots. However, in the test shots it was found that pieces of the shear disks were inevitably launched down range and struck the target. Three steps were taken to eliminate the burst-diaphragm problem and to improve the gas pressure seals. Seals and diaphragms were made from 304 SS. The diaphragm was inscribed with cross V-grooves. Last, a new

component was added--a burst-diaphragm die made from 4340 steel. Figures 7-9 show the new assembly that fitted between the launch tube and high-pressure section.

The burst-diaphragm was fabricated from 1.22-mm-thick 304 SS into disks of 56 mm diam. The disks had milled grooves on one side in the form of a cross with various web thicknesses and groove lengths. Various groove thicknesses and lengths were used in several tests to determine the effect of groove dimensions on velocity. Milled grooves (when subjected to a pressure that causes them to fail at the thinner web of the groove) formed a four-piece petal. To keep these petals from breaking off (which the first few did because of a sharp 90° base area), the burst-diaphragm die was designed with a rounded forming base and a tapered hole which was sized at the launch tube end of the caliber of the launch tube bore. This die eliminated the problem of a petal piece breaking away and traveling down range into the target area.

The pressure seals for both ends of the high-pressure section were also fabricated from 304 SS. The seals themselves were flat disks (1.22 mm thick) machined to diameters which would allow them to be inserted into the high-pressure section ends. After a few launches there was still gas leakage at

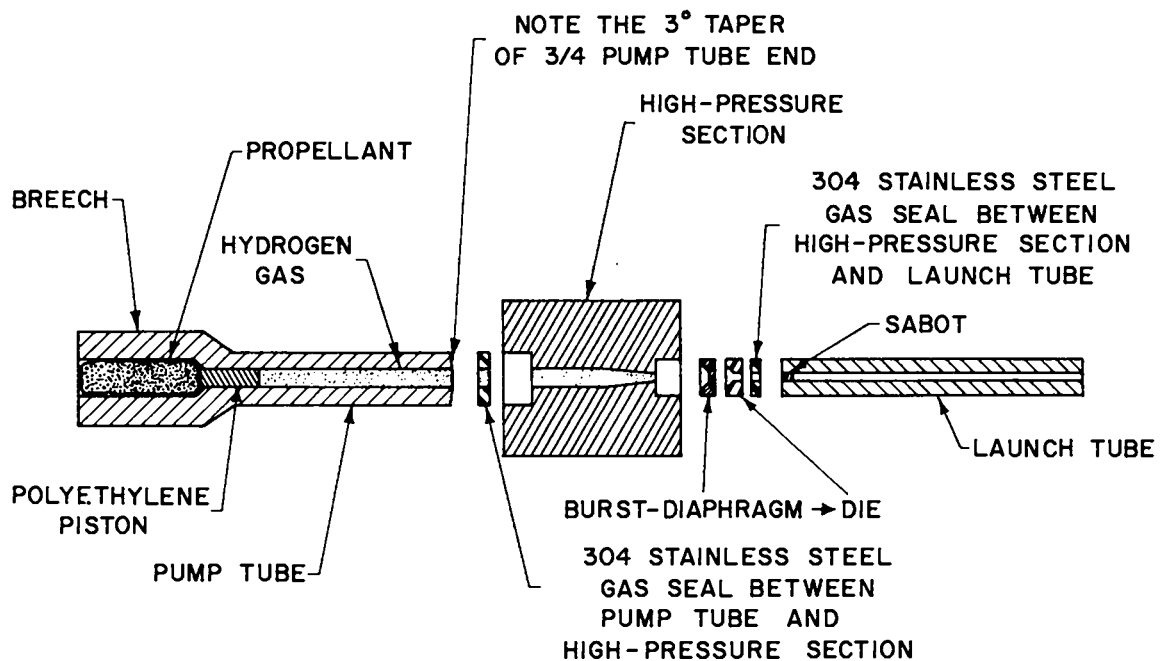


Fig. 7. Schematic of basic light-gas gun with gas seals and burst-diaphragm locations.

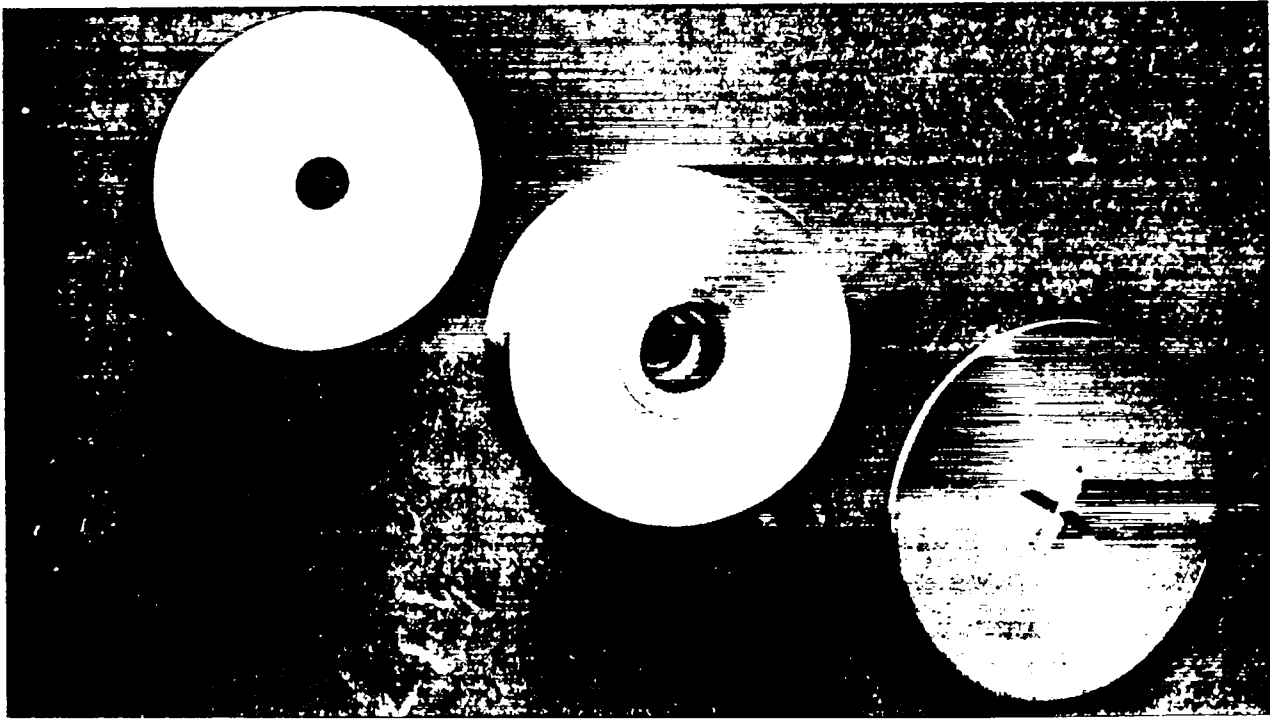


Fig. 8. Burst-diaphragm, die, and seal disk.

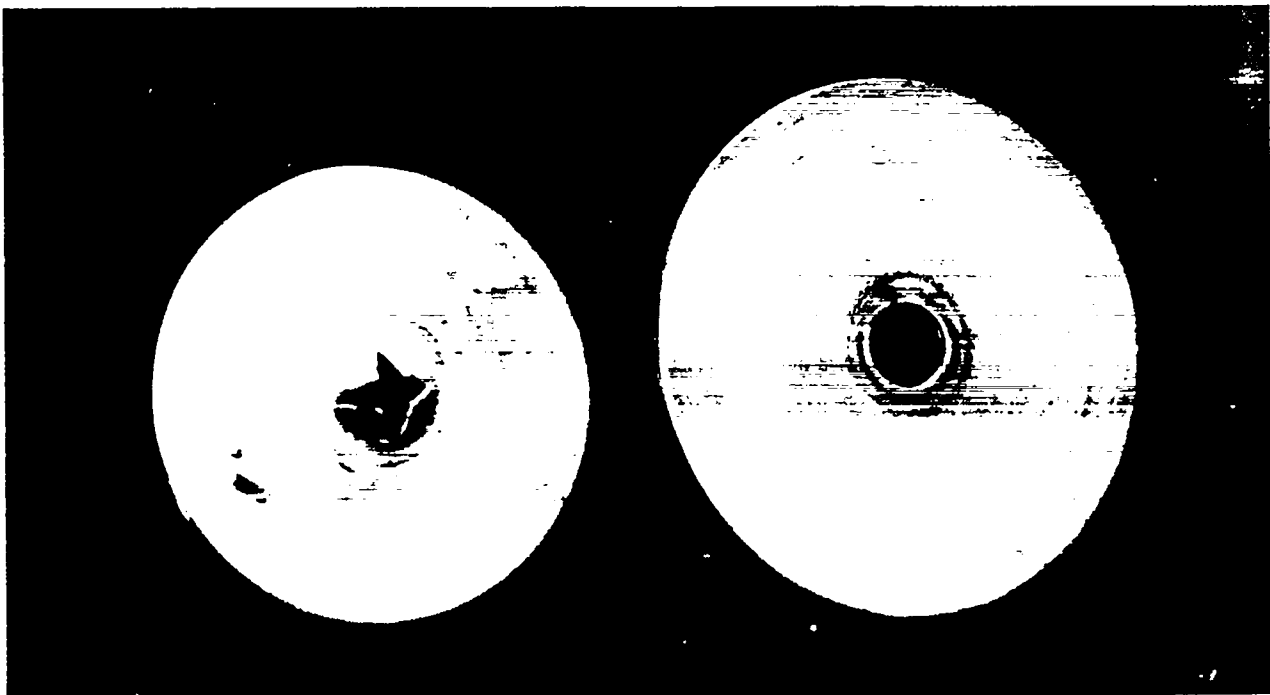


Fig. 9. Burst-diaphragm and seal after a shot.

the seals. To eliminate this leakage, the pump tube high-pressure end was modified. A shoulder 6.5 mm wide next to the bore was left flat and perpendicular to the tube bore. The remainder of the face was machined to an angle of 3° from the perpendicular. The shoulder around the bore acted as a high-pressure seal which mated to the high-pressure section stainless steel seal surface.

c. Projectile Launching. In order to launch small spheres from the light-gas gun, it was necessary to accelerate them inside a sabot that was stopped before reaching the target. As the projectile and sabot exit from the launch tube, the sabot must separate cleanly from the projectile without interference to the projectile flight path. A four-piece serrated lexan sabot was machined such that the projectile could be seated in the nose of the sabot (Fig. 10). About 2.1 m down range, just before the target tank, a sabot stripper or stopper plate and a shorting-pin (used to trigger various instrumentation units) was mounted. An exploded view of this assembly can be seen in Fig. 11.



Fig. 10. Left: Serrated sabot with 1.4-mm glass bead in pocket.
Right: Expected in-flight attitude.

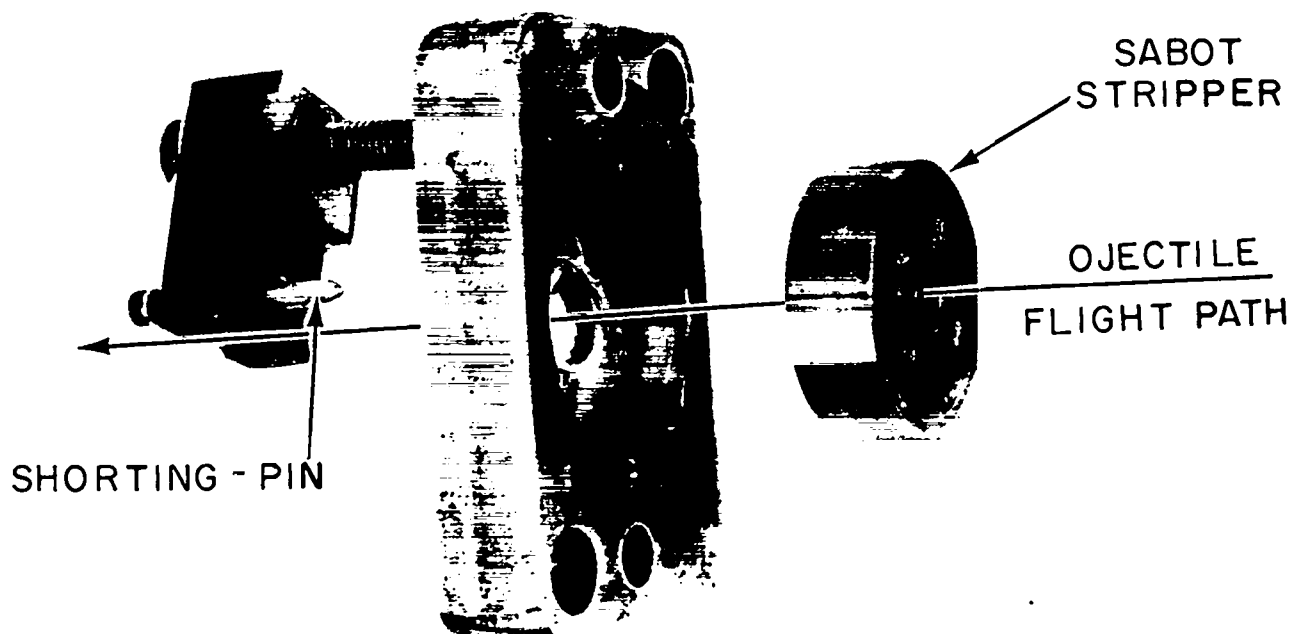


Fig. 11. Sabot-stripper with shorting pin.

Although the shots were conducted in a vacuum, enough gas (air or argon) was left in the blast/target tank (between 20 and 25 mm Hg) to force the four-piece sabot to open in its down range flight, so that its separation at impact with the sabot stopper plate was about 40 mm in diam. As seen in Fig. 12, radiographs of the sabot in flight revealed that it opens backwards rather than forward as illustrated in Fig. 10. In most shots, including all shots with heated targets, the gas in the range was argon. The 10 mm-14 mm hole through the stopper plate allowed the projectile to proceed unimpeded down range to the target. The target was usually placed about 150 mm behind the stopper plate.

Full-density spherical projectiles made of glass, copper, aluminum, and cadmium were accelerated to velocities ranging from 4.43-7.56 km/s in the sabot. The glass projectiles were obtained from Cataphote Division of Jenco Corporation. They were Class III spacer-graded unispheres with $\rho = 3.99 \pm 0.05 \text{ Mg/m}^3$. Each bead was checked for diameter and weight prior to each shot. The copper projectiles were made from on-hand copper rod, and the aluminum projectiles were on-hand aluminum spheres. The cadmium projectiles were made by remelting pure cadmium shot purchased from the Alfa Division of Ventron Corporation.

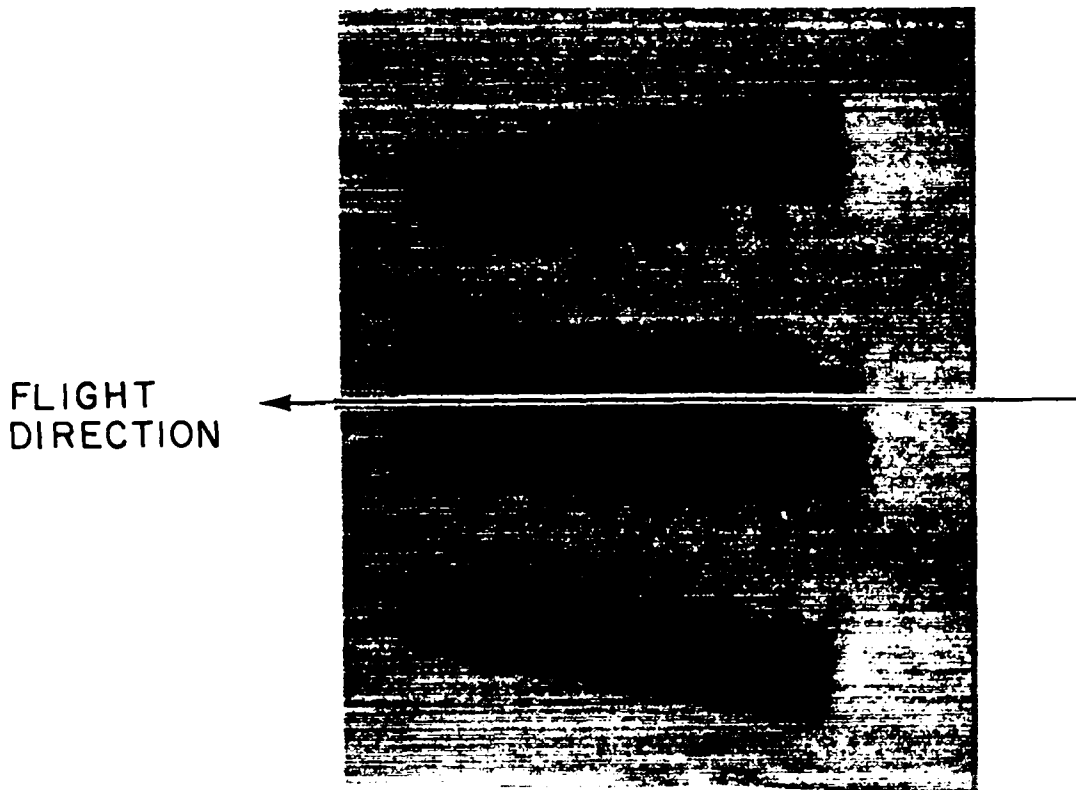


Fig. 12. Radiograph of sabot opening in flight.

The first approach tried in this program was multiple bead launch, in order to quickly determine ballistic limits. Submillimeter-size beads were used to simulate meteoroid energies. In half a dozen test shots it was demonstrated that multiple launch was not feasible; the beads always clumped together.

Thereafter, the approach taken was to launch larger beads at thick targets in order to determine cratering and penetration parameters. Larger beads were used because larger craters could be more precisely characterized and because the probability of shot failure was several times less for beads of diameter >1 mm. (Shot failure usually was caused by failure of the projectile to pass cleanly through the sabot plate hole or by fragments from the sabot or sabot plate striking the target.)

2. Target Facilities. Most of the impact experiments were performed with the target heated to 775 K. Figure 13 shows the heating unit and mounting in which targets could be heated to any desired temperature from room temperature to over 975 K. The figure shows the target beneath the heating chamber ready for impact. During heating, the target was raised into the chamber. Both the heating chamber and target holding fixture were insulated from contact with

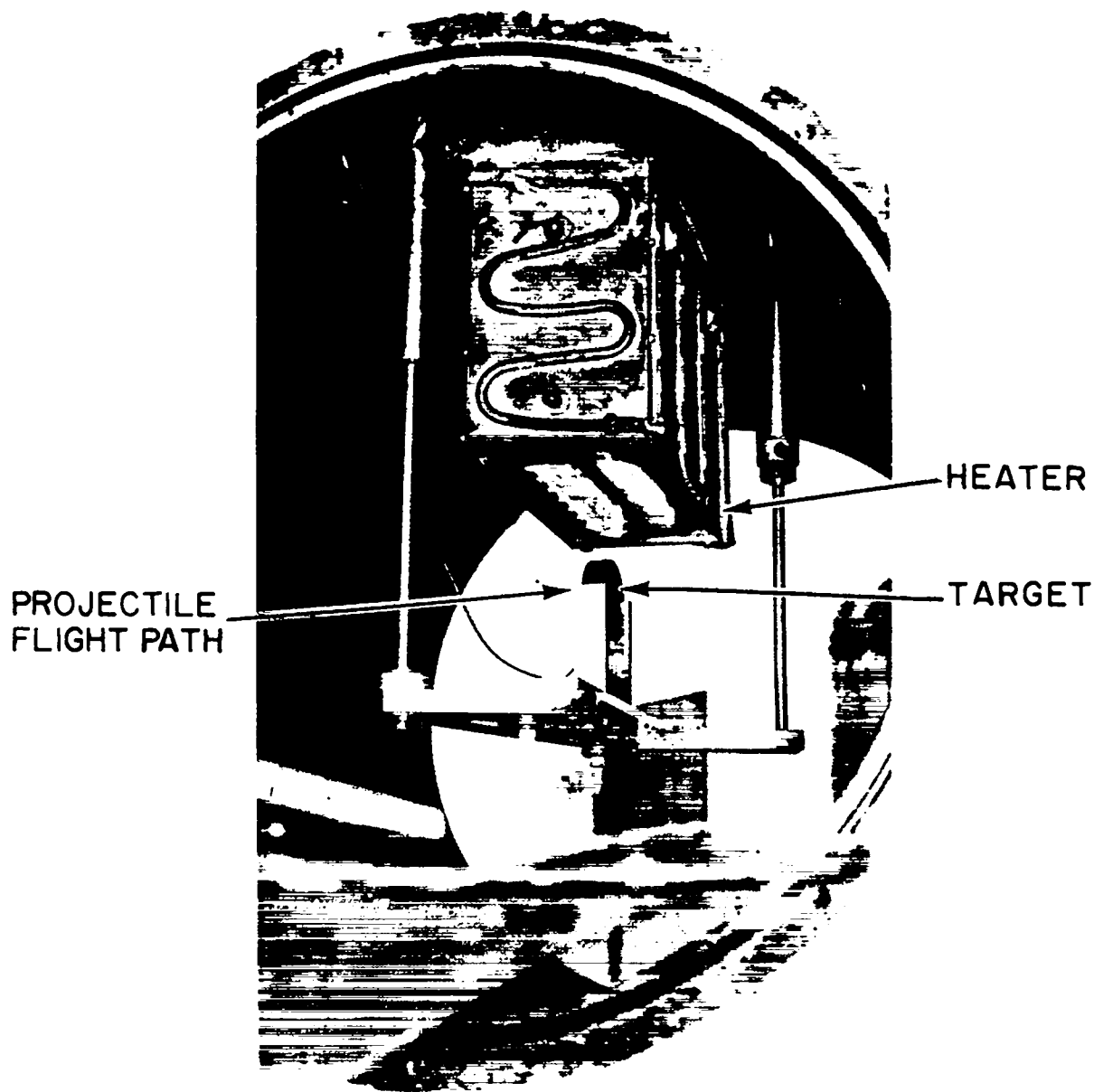


Fig. 13. Target heating apparatus with target in position for impacting.

surrounding range hardware. Temperature was measured with a thermocouple placed on the surface of the target. Typically, the target was withdrawn from the chamber at 825 K, and by the time the gun was fired its surface temperature measured 725 K.

During the program, two beryllium targets were impacted with 1.6-mm-diam copper projectiles. For these shots, additional safety precautions were required to protect personnel and equipment from debris and dust particles emitted from the target surface after impact. Rubber gloves were worn whenever the targets were handled. Other required personnel equipment included dust resistant protective breathing masks and throw-away lab coats. Re-pressurization of the target tank required ~ 1 h of postimpact time. A special encapsulating target holder with removable (throw-away) mounting and spall ends and a 75-mm length of tubing was machined from aluminum to contain the beryllium residue and fragments. A 9.5-mm-diam hole was drilled through the front (spall) end to facilitate projectile entry. Figure 14 shows this special fixture. This fixture could be heated with the standard chamber by rotating the chamber 90° from its orientation in Fig. 13.

3. Instrumentation. The complete range instrumentation employed during the initial test phase is shown schematically in Fig. 15. Laser-triggered flash x-ray units were used to obtain radiographs of the projectiles in the blast tank. An annular mylar foil switch detected the arrival of the projectile at the sabot stripper plate. The foil switch triggered a flash tube that provided illumination for the high-speed framing camera. Projectile velocity was computed from three redundant measurements: the time interval between the first laser detector signal and the arrival at the sabot plate; the time interval between sabot plate arrival and target impact; and the time-position data from the framing camera record.

The flash x-rays were 150 kV. The purpose of the radiographs was to increase the precision of the velocity measurement and to diagnose sabot functioning. The framing camera was a Beckman and Whitley Model 300 (B&W 300). This is a continuous-access camera that takes 48 frames. It was normally operated at between 1.2 and 2 million frames per second. The framing camera records provided velocity data and information on the debris clouds. The framing camera employs 8 X 10 film. Kodak No. 7302 fine-grain, positive film was used. Figure 16 shows a sample record. The projectile, starting in frame 22, can be seen to move toward and impact the target. Figure 17 is a blow-up of frames 21-44.

Measurement of projectile velocity was initially very troublesome. Radiographic confirmation of projectile position at the time the laser stations were triggered was very difficult to obtain. Experimentation with different

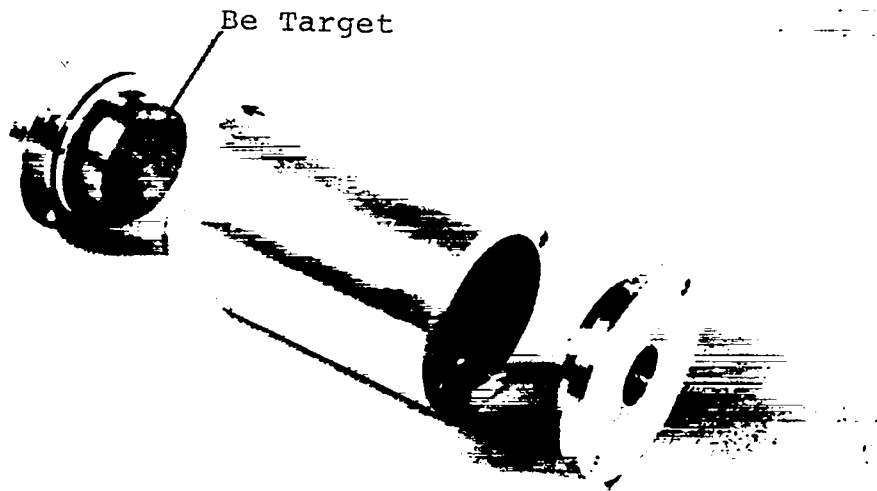


Fig. 14. Target chamber used for beryllium targets.

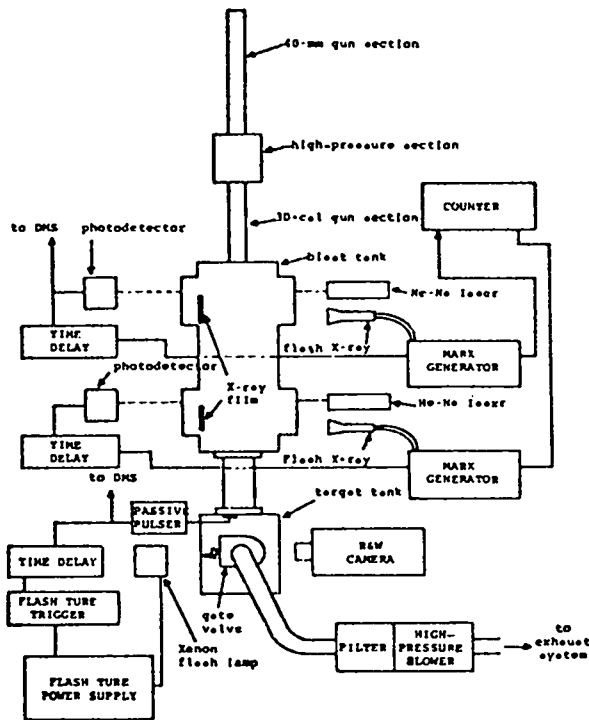


Fig. 15. Diagram of range instrumentation employed in initial technique-development shots.

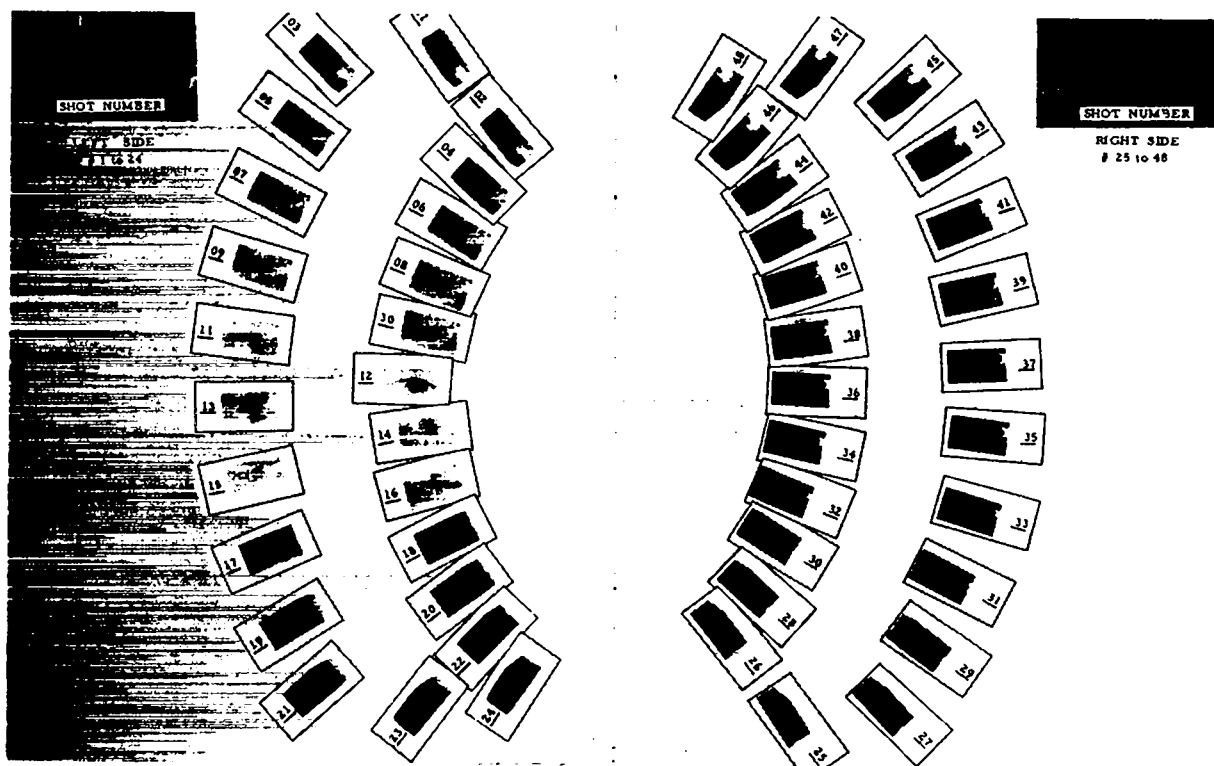


Fig. 16. Framing camera record from Shot 96.

delay times between laser stations were vulnerable to pretrigger from gas or blow-by debris. No contacting technique could be used to determine projectile position without damaging the sabot. During a sequence of shots, several techniques were evolved to more reliably measure projectile velocity.

First, the foil switch at the sabot plate was replaced with a contact switch closed by the shock wave induced in the sabot plate by sabot impact. The contact switch consisted of a steel screw tightened against a 0.13-mm-thick sheet of Mylar placed on the back surface of the sabot plate. The switch was connected to a passive-pulser unit, which delivered a several-hundred-volt signal when its input was shorted. Shock breakout ruptured the Mylar and established electrical contact between the pin and sabot plate. With this system, false triggers were effectively eliminated. Figure 11 illustrates how this unit was assembled.

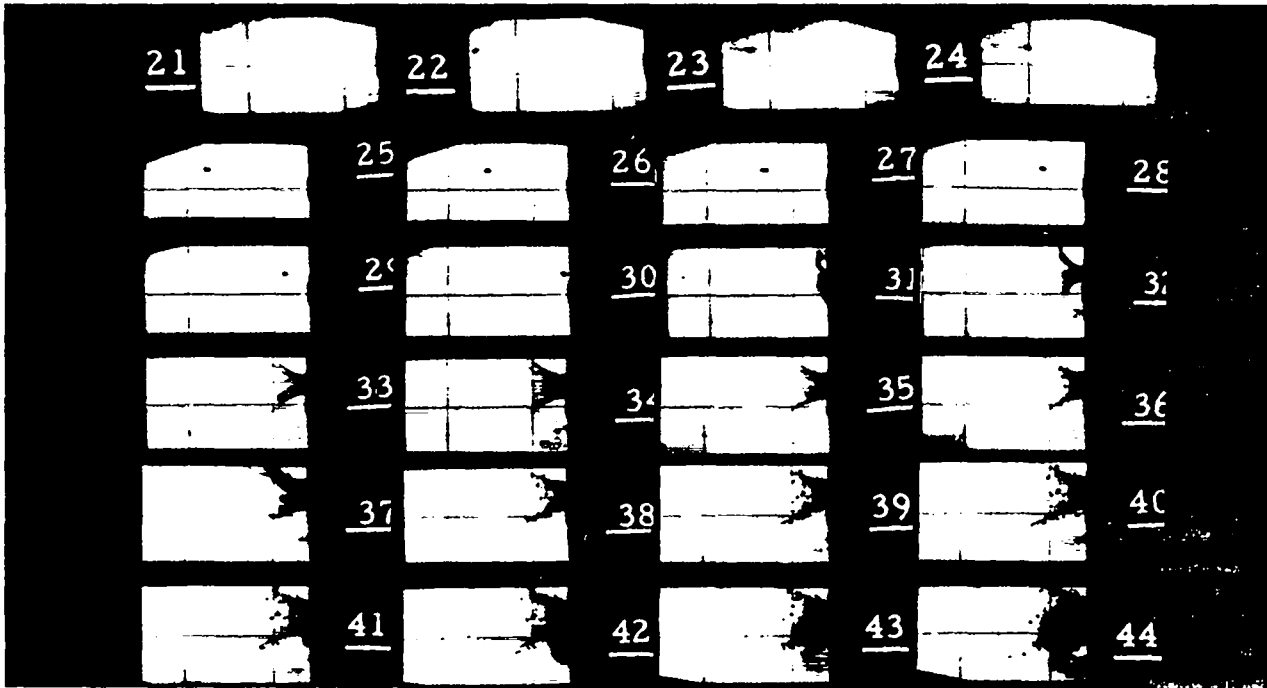


Fig. 17. Enlargement of frames 21-44 from Fig. 16.

Redundant velocity data were obtained with the B&W 300 camera. It was first employed in Shot No. 75; we were very anxious to check that the velocity measurements previously obtained were not in error due to motion blur. Only half a sabot plate was used to make the projectile visible to the camera. The other half of the sabot traversed the B&W 300 field of view, permitting measurement of velocity by tracking the sabot fragments. Figure 18 illustrates the sabot plate arrangement for one of those shots. It was found that the velocity was a little lower than had been inferred from the previous data. This led to the redesign of the high-pressure seals, as discussed previously.

Beginning with Shot No. 76, the signal from the sabot plate was used to stop a digital oscilloscope that recorded the two photomultiplier (PM) tube signals. In Shot Nos. 76-85, the first PM tube recorded the muzzle flash. In most shots, the arrival of the projectile at the laser station could clearly be identified. Figure 19 shows a typical example. The muzzle flash record

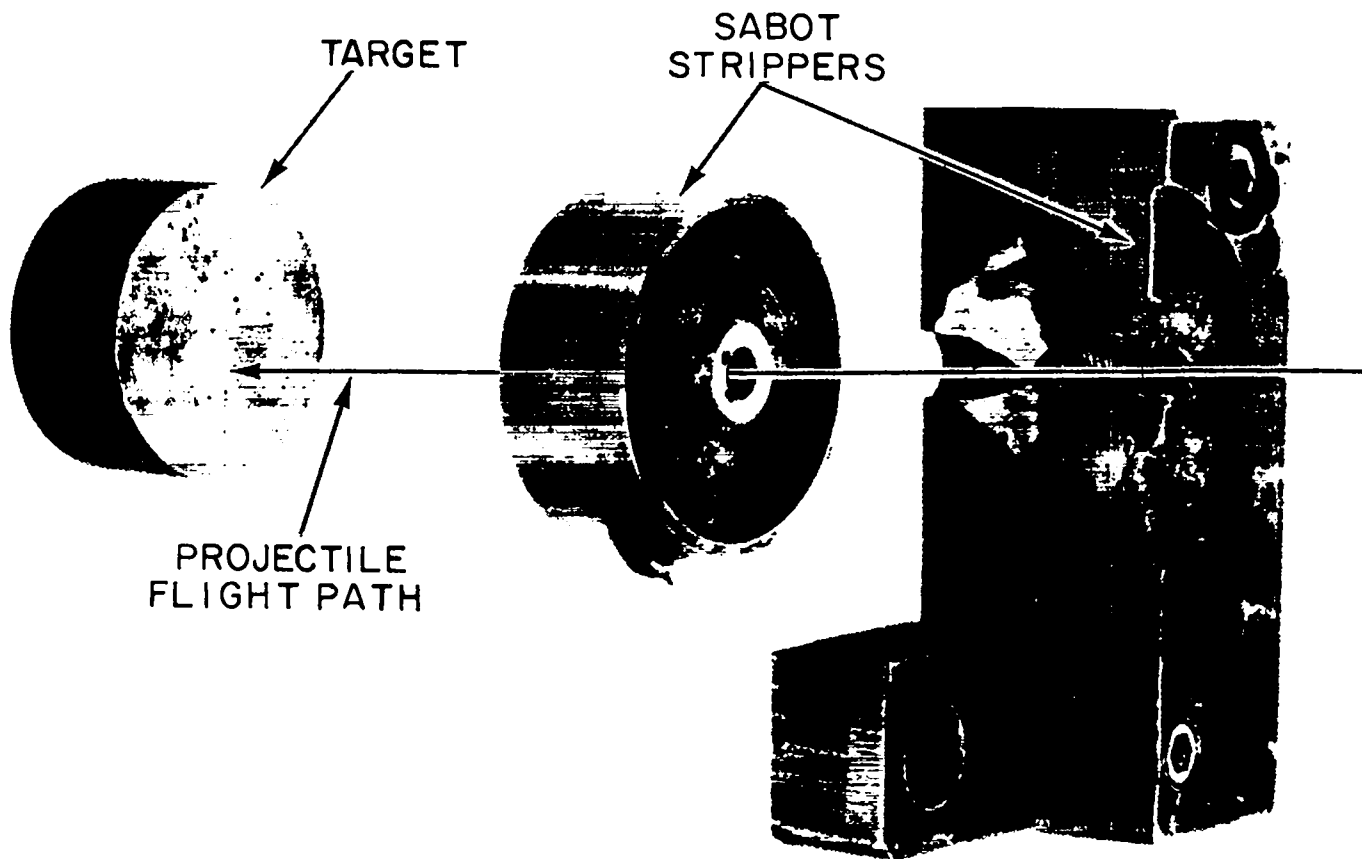


Fig. 18. Sabot plates and target from Shot No. 78.

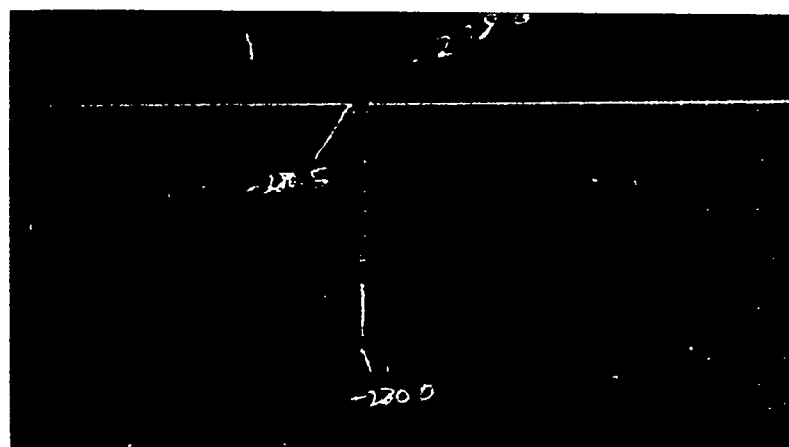


Fig. 19. Portion of record showing typical cut-off of second laser beam by projectile and other material launched by gun. The passage of the projectile can be identified as the short downward spike. Data from Shot No. 84.

was found to exhibit a great deal more structure than anticipated. Figure 20 shows a typical example. Unfortunately, analysis of a suite of records showed that no single feature of the muzzle flash signal could be correlated with exit of the projectile. Eventually, the first PM tube was once again used to view a laser. It was found that precaution had to be taken to avoid blinding this tube by the muzzle flash. The record from the second laser station could not be clearly interpreted in some shots because the sabot had partially opened and did not completely block the beam. This defect was later corrected by using a three-passage laser ladder at the second station.

In most data shots, the B&W 300 camera was used to view the projectile. Beads 1 mm in diam and larger were visible as in Fig. 16. Thus, in most data shots, two redundant measures of impact velocity were available. An empirical correction factor was developed for the time interval between impact on the sabot plate and closing of the contact switch. With this correction, agreement between framing camera data and the other time-of-flight measurements were generally satisfactory.

Crater volumes in the sabot plate also provide a very rough check on projectile velocity. In some instances of gross instrumentation failure, sabot plate craters were also used to bound projectile velocity. Data for sabot plate craters (for two different sabot plate materials) are shown in Fig. 21.

B. Target Materials

Most of the targets impacted in this study were commercial-pure, Grade 2 Ti machined from either 50-mm-diam bars or an 11-mm-thick plate. The chemical analyses of these materials are listed in Table I. These targets

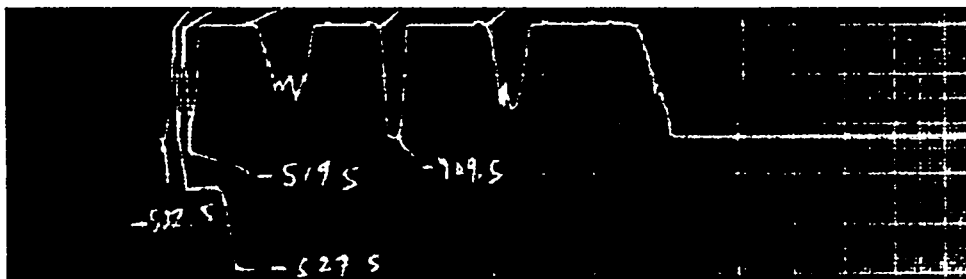


Fig. 20. Typical record of muzzle flash from light-gas gun.
Data from Shot No. 79.

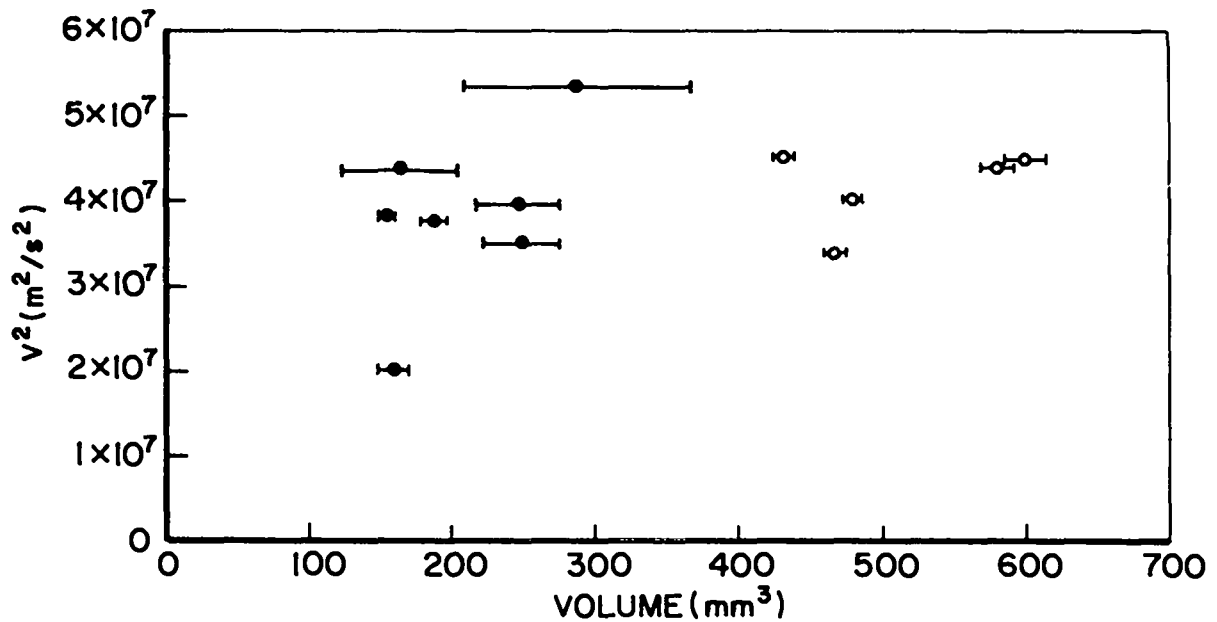


Fig. 21. Volumes of craters made in steel sabot plates by 0.15 g-sabot segments. Open circles were RC 20 hardness, closed circles were RC 30.

were measured to have Rockwell C (RC) hardnesses ranging from 23-25 (Rockwell B(RB) 82-90). The preshot microstructure of the titanium bar stock seen in Fig. 22 shows a significant number of impurity stringers extending parallel to the centerline of the bar. The preshot microstructure of the plate stock was similar except that it did not contain a noticeable number of stringers. Their absence probably results from the lower oxygen and iron content of the plate. Grade 2 Ti sheets with a variety of surface treatments were also impacted. The surface treatments included an embossed diamond pattern, a shot-blasted surface, and two different emissivity coatings, zinc orthotitanate and amorphous carbon (D-111). The projectiles impacted the side with the emissivity coatings and opposite the embossed and shot-blasted surfaces.

Because titanium has very low mechanical strength at 775 K and above, we performed impact experiments on two different high-temperature titanium alloys. One alloy was Ti-5Al-2.5Sn and the other was Ti-6Al-2Sn-4Zr-2Mo-0.25Si (Ti-6242Si). The chemical compositions of the plate stocks from which the impact samples were machined are listed in Table I. The Ti-5Al-2.5Sn plate was a transverse section taken from a forged bar, while the Ti-6242Si plate

TABLE I
CHEMICAL ANALYSIS OF TARGET MATERIALS

Description	Chemical Analysis (Wt %)									
	C	N	H	O	Fe	Al	Sn	Zr	Mo	Si
Grade 2 Titanium Bar	.0080	.0076	.0004	.2600	.23	-- ^a	--	--	--	--
Grade 2 Titanium Plate	.016	.0090	.0078	.1040	.10	--	--	--	--	--
Ti-5Al-2.5Sn	.0090	.0090	.0070	.0850	.0320	5.05	2.31	--	--	.0180
Ti-6242Si	.0095	.0210	.0065	.0850	.0400	5.99	1.97	4.05	2.01	.2000
Beryllium	.0170	.0200	--	.625	.0700	.0700	<.003 ^b	<.08	<.003	.0220

Mg = .0400, Al = .0070, Ca = .0006, Ni = .0140, Mn = .0070, Cu = .0080

a -- means not determined.

b < means less than the stated detection limit.

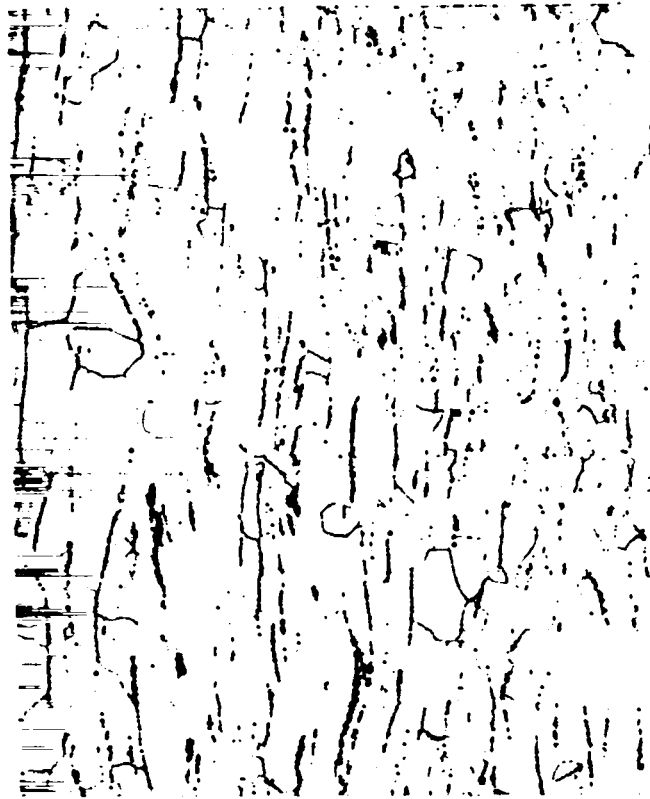
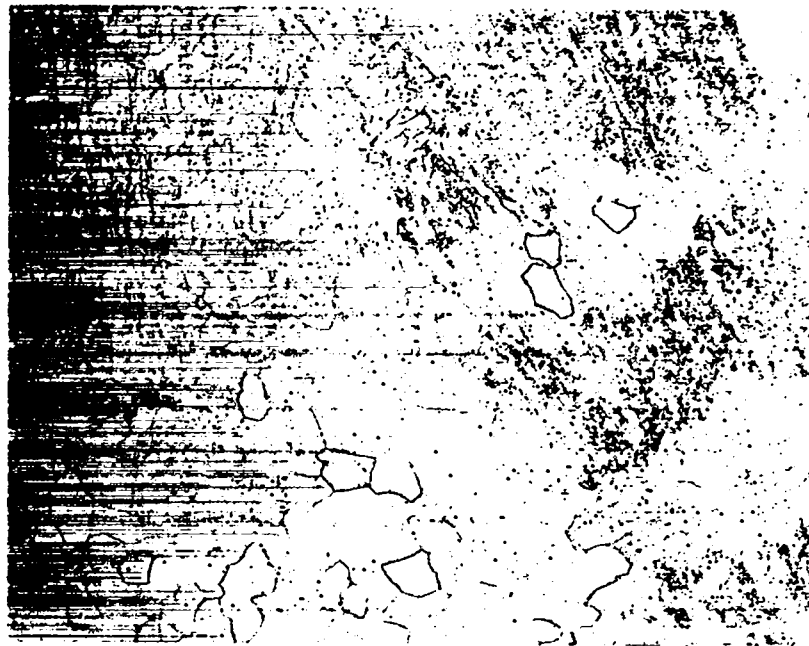
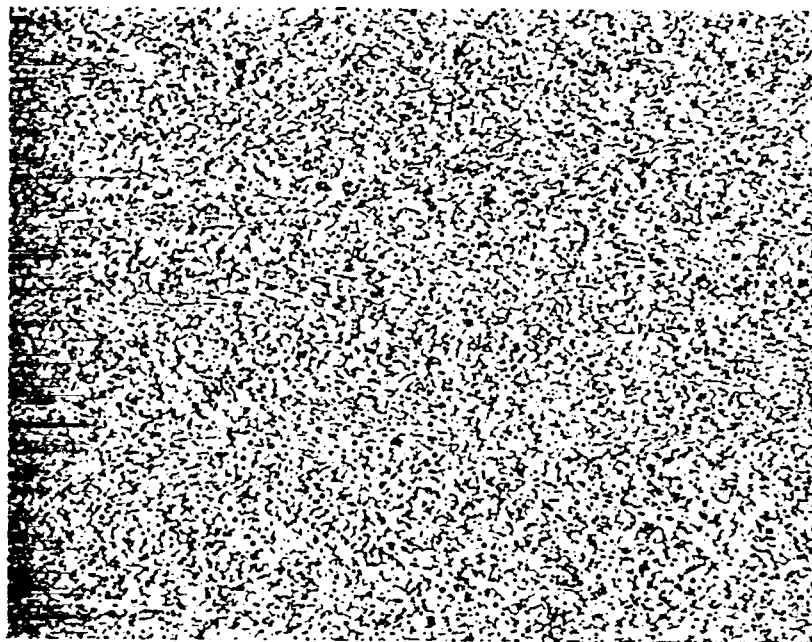


Fig. 22. Preshot microstructure of Grade 2 titanium bar used in impact tests, longitudinal section.



(a)



(b)

Fig. 23. Preshot microstructures of (a) Ti-5Al-2.5Sn and (b) Ti-6242 Si used in impact studies, longitudinal sections.

was a transverse section taken from an extruded bar. Both plates were supplied by RMI. The preshot microstructure of these alloys can be seen in Fig. 23. Here, it can be seen that Ti-5Al-2.5Sn is an alpha-titanium alloy, while Ti-6242 Si is an alpha-beta alloy. Both alloys had an RB 82 hardness.

In order to determine whether beryllium produced today possesses better hypervelocity impact behavior than in the past, we performed impact experiments on samples taken from recently produced weapons grade stock. The targets were 12.7-mm thick by 30.5-mm diam. Chemical analysis of the target stock is listed in Table I, and the preshot microstructure is seen in Fig. 24.

IV. EXPERIMENTAL RESULTS

Data were obtained for impacts onto thick targets of Grade 2 Ti, Ti-5Al-2.5Sn, Ti-6242Si, and beryllium. Impacts were made onto Grade 2 Ti targets maintained at 295, 475, and 775 K, while all other target materials were impacted at 775 K. The crater volume data spanned two orders of magnitude in projectile energy. Perforation velocities were determined for thin titanium targets at both 295 and 775 K. The perforation data were taken to establish the validity of predictions based on thick target response. Effects of various surface treatments and coatings on titanium were also studied.

Table II lists data from the successful shots. Not all of these data were retained for analysis. In several cases, the impact craters were judged false on the basis of excessively high or low depth-to-diameter ratio ($p/D = 0.5$ for a hemisphere) or because the crater was not symmetric. In some earlier shots, rear-surface target bulge also invalidated crater data; in later shots, backup plates were always used.

Crater volumes were determined by backfilling the craters to the preimpact surface with 0.1-mm glass beads. The volume of the beads was measured using tiny graduated cylinders derived from precision syringes. Crater depths were determined from multiple measurements with a sharpened depth micrometer, and occasionally from metallographic sections. Uncertainties in the given table were derived from repeated measurements. The crater diameter, D , was calculated from the formula for the volume of half an oblate spheroid:

$$V = \pi p D^2 / 6 \quad . \quad (7)$$

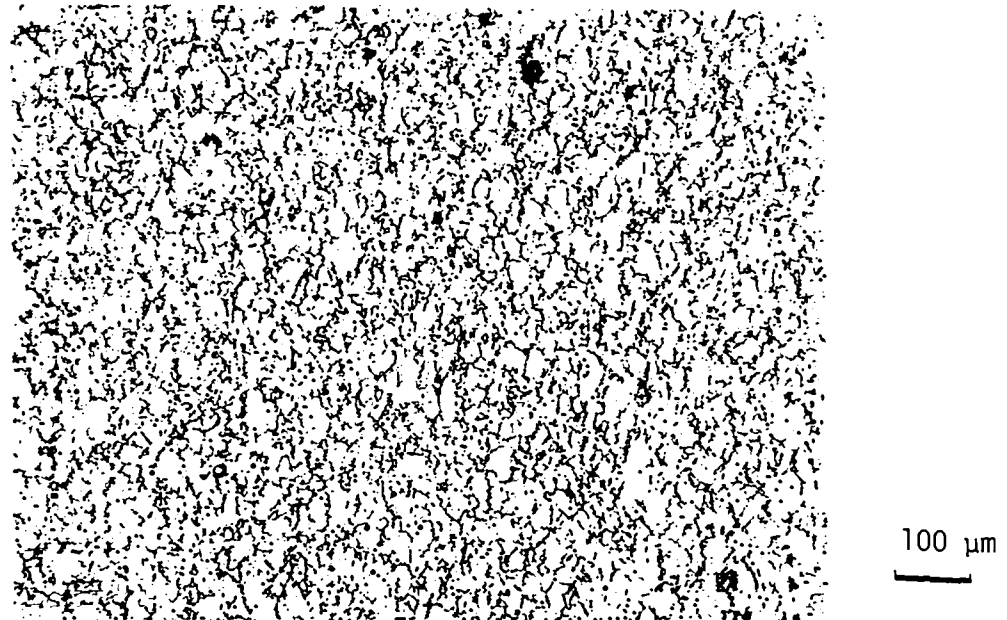


Fig. 24. Preshot microstructure of beryllium used in impact tests, longitudinal section.

A. Thick Targets

1. Grade 2 Titanium. In general, the impact craters formed in pure titanium appeared "scaled" on their interior surfaces. This phenomenon can be seen in cross section, especially in Figs. 25(a) and 26(a). Here, we see that there are loosely attached "scales" on the crater sides. Occasionally, partially detached platelets were found on the craters. These features result from the formation of adiabatic shear zones as can be seen especially in the higher magnification photomicrographs in Figs. 25 and 26. As noted in Figs. 27 and 28, the adiabatic shear zones are much less pronounced in titanium that was impacted at 775 K. There is a band of intense plastic flow ~ 1 mm thick around all the craters. This region is capped with a microstructure that strongly suggests that the inside surfaces of the craters were molten during impact. This resolidified structure is best shown in Fig. 27(c).

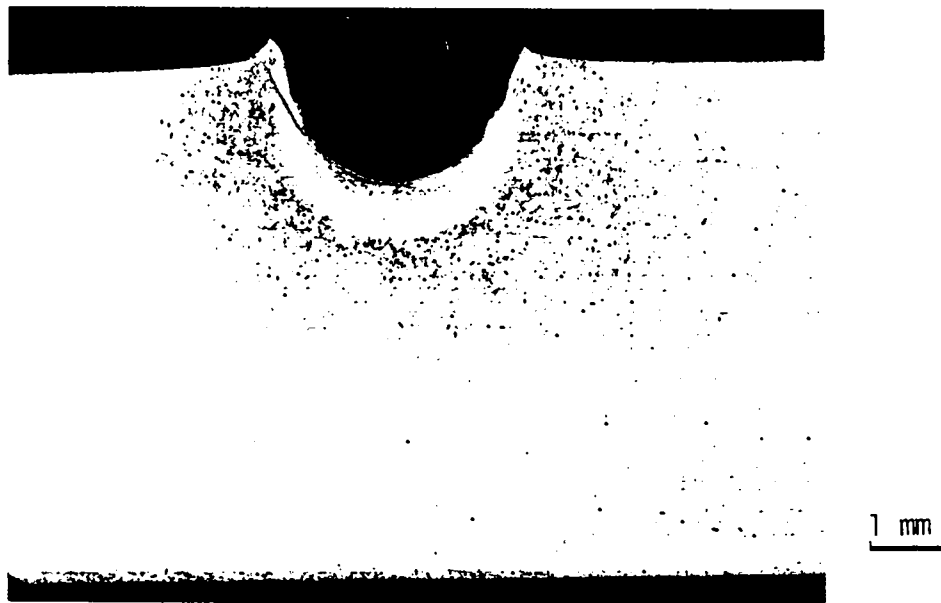
Incipient spall was observed in many of the plate targets that had been mounted on a backing plate. A typical incipient spall region can be seen in Fig. 27(a). A higher magnification view of a portion of the region is given

TABLE II
IMPACT DATA

SHOT No.	PROJECTILE MAT'L	PROJECTILE			TARGET			CRATER		REMARKS
		d (mm)	m (mg)	u (km/s)	TEMP (K)	t (mm)	p (mm)	V (mm ³)	p/D	
76	G	0.5	NM	5.04 ± 0.07	295	2.54	1.09	3.85	0.419	Target bulged
78	G	0.5	NM	> 5.4	295	25.4	NM	NM		
79	G	0.5	NM	4.50 ± 0.05	295	25.4		2.57 ± 0.12		Eccentric crater
82	G	0.5	NM	5.80 ± 0.05	295	7.44	0.80 ± 0.04	1.13 ± 0.09	0.487	
84	G	1.0	2.23	6.44 ± 0.12	295	7.49	1.70 ± 0.03	11.92 ± 0.09	0.464	
87	G	1.0	2.23	6.66 ± 0.07	295	9.30	0.69 ± 0.03	1.91 ± 0.06	0.300	Rejected, for p/D
88	Cu	1.59	21.16	5.62 ± 0.06	295	8.43	4.72 ± 0.18	85.1 ± 3	0.804	Crater damaged, target bulged
89	Cu	1.59	20.84	5.80 ± 0.04	295	13.26 ^a	4.54 ± 0.18	95.3 ± 1.2	0.717	
90	G	1.0	2.225	4.43 ± 0.06	295	8.13 ^a	1.36 ± 0.04	3.66 ± 0.08	0.599	Crater damaged
91	G	1.0	2.23	4.88 ± 0.29	295	8.13 ^a	0.91 ± 0.03	5.49 ± 0.10	0.268	Rejected, for p/D
94	Cu	1.59	21.02	5.54 ± 0.08	475	13.28 ^a	4.66 ± 0.17	93.7 ± 0.7	0.752	
(95) ^b	G	1.0	NM	6.13 ± 0.04	295	2.78				Perforated
96	G	1.40	4.444	7.30 ± 0.06	295	14.61 ^a	1.87 ± 0.08	22.3 ± 0.8	0.392	Eccentric crater
98	G	1.40	5.908	6.28 ± 0.15	775	12.52	3.92 ± 0.03	60 ± 7	0.725	Double impact
99	G	1.40	5.716	6.16 ± 0.15	775	12.78	2.64 ± 0.06	40 ± 5	0.491	
103	G	1.35	5.606	6.15 ± 0.11	775	11.05	1.30 ± 0.03	8.2 ± 0.05	0.375	Crater too small
104	G	1.45	6.432	6.58 ± 0.02	775	11.05	2.90 ± 0.05	55.3 ± 1	0.481	Secondary crater
105	G	1.45	6.448	7.08 ± 0.02	295	14.61	2.42 ± 0.02	34.5 ± 1	0.464	
130	Cu	1.59	20.5	6.79 ± 0.05	775	10.8 ^a	5.43 ± 0.10	162.5 ± 2	0.718	Eccentric crater
131	Cu	1.59	21.80	7.35 ± 0.05	775	10.8 ^a	6.38 ± 0.03	205 ± 5	0.815	
132	Cu	1.59	22.66	7.44 ± 0.05	775	10.8 ^a	6.22 ± 0.02	120 ± 2	1.025	
133	Cu	1.59	20.00	7.29 ± 0.05	775	10.8 ^a	5.17 ± 0.04	185 ± 2	0.625	
134	Al	2.38	20.0	7.56 ± 0.04	775	10.8 ^a	4.17 ± 0.04	156 ± 5	0.493	
135	Cu	1.59	18.40	6.59 ± 0.05	775	7.25	5.83 ± 15			Spall double impact
(136)	Cu	1.59	19.3	6.59 ± 0.07	775	7.24				Perforated
(137)	G	1.42	4.604	6.60 ± 0.05	775	3.94	2.96 ± 0.03			Spalled
138	Cu	1.59	20.02	6.48 ± 0.5	775	8.26				Impacted by debris
140	Cu	1.59	19.50	6.7 ± 0.6	775	8.26				Impacted by debris
(141)	Cu	1.59	21.04	6.70 ± 0.5	775	8.26				Perforated
(142)	G	1.4	5.988	6.30 ± 0.22	775	3.56	1.42 ± 0.02			Target bulged
(143)	G	1.4	4.39	6.8 ± 0.4	775	3.94				45° Impact, Perforated
(144)	G	1.4		7.12 ± 0.02	775	3.56				Perforated
147	Cd	1.65	20.8	6.18 ± 0.05	775	10.52 ^a	5.26	130 ± 2	0.766	
150	Cu	1.56	22.06	6.96 ± 0.03	775	15.49 ^a	4.53	110 ± 3	0.665	Ti-5Al-2.5Sn
151	Cu	1.56	21.34	6.59 ± 0.03	775	25.07 ^a	4.53	121 ± 2	0.634	Ti-6242Si
(152)	G	1.4	4.62	6.0 ± 0.5	775	3.96	3.05			Double layered target, shot blasted
(154)	G	1.4	4.62	6.59 ± 0.05	775	0.69	2.15 ± 0.05			Double layered target, zinc orthotitanate
(156)	G	1.4	4.62	6.60 ± 0.3	295	0.69	2.29 ± 0.05			Double layered target, D-111
(158)	G	0.5	0.300	7.17 ± 0.28	295	0.56				Perforation shot-blasted
159	Cu	1.6	22	7.11 ± 0.05	295	12.65	5.64 ± 0.11			Be, target shattered
160	Cu	1.6	22	6.84 ± 0.05	775	12.65	6.94 ± 0.14			Be, target shattered

^a Backing plate used.

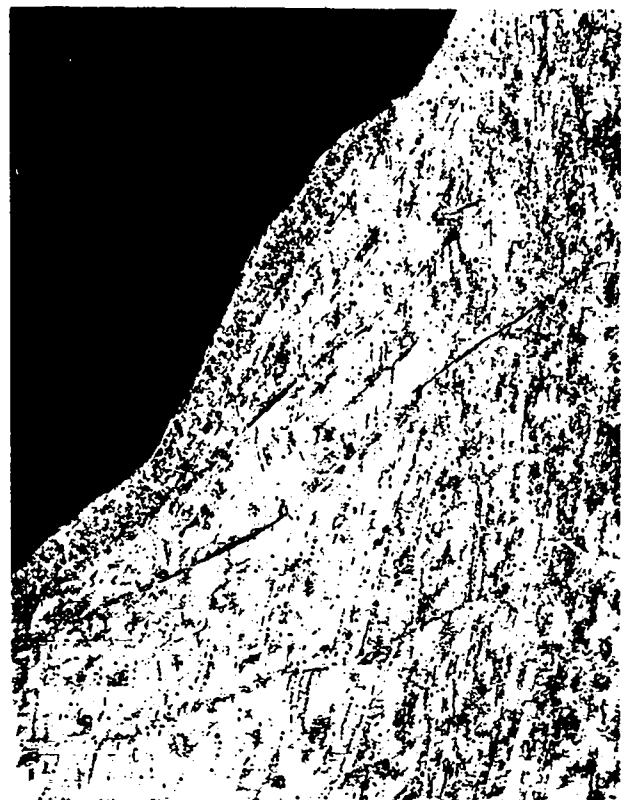
^b () shot numbers indicate thin impact targets.



(a)



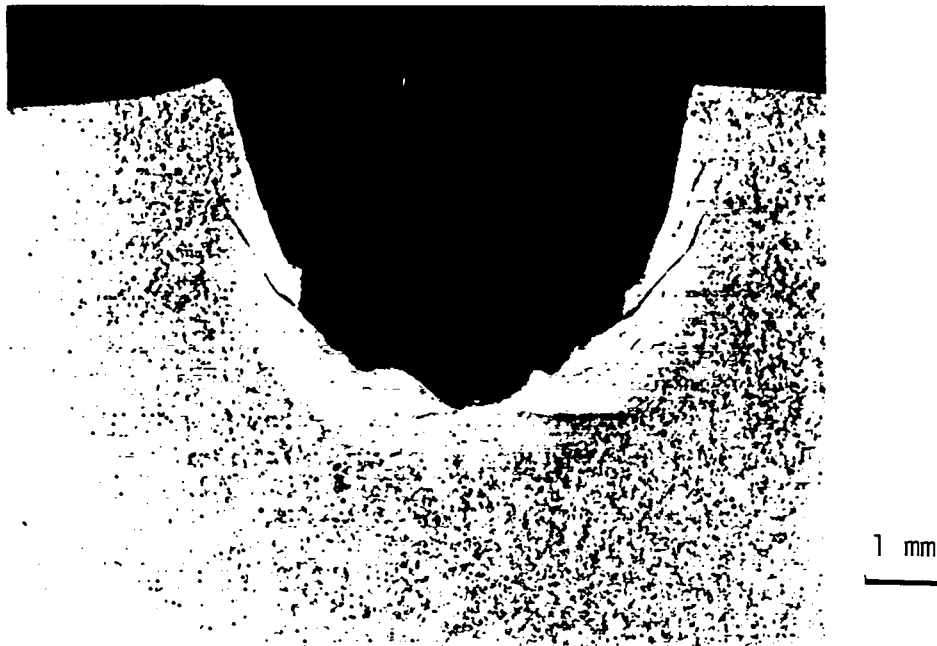
(b)



(c)

0.1mm

Fig. 25. Titanium bar impacted at room temperature with a glass bead (Shot No. 84): (a) crater cross section, (b) crater bottom, and (c) right side of crater.



(a)



(b)



(c)

0.1 mm

Fig. 26. Titanium bar impacted at room temperature with a copper sphere (Shot No. 89): (a) crater cross section, (b) crater bottom, and (c) right side of crater.



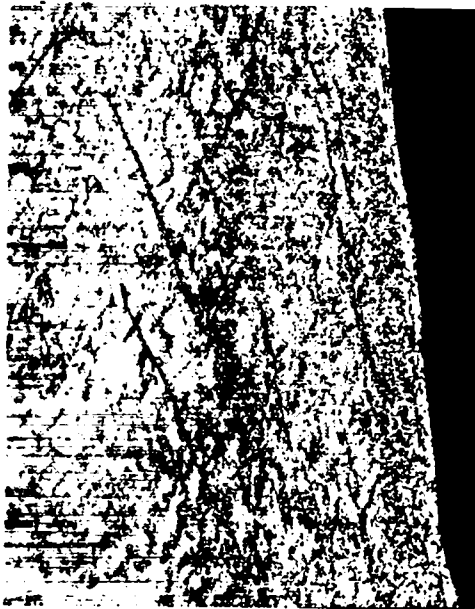
(a)

1 m



(c)

40 μm



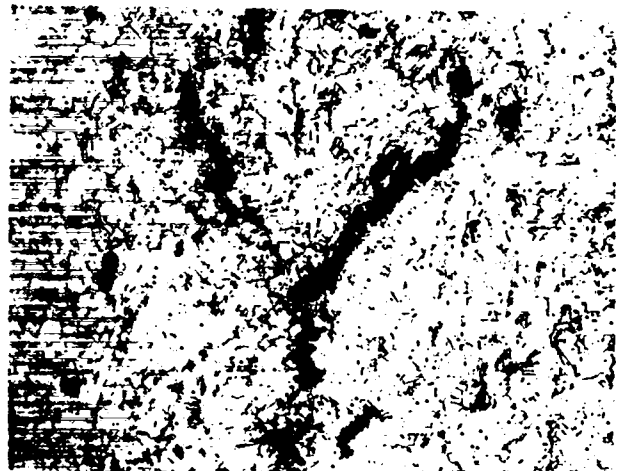
(b)

0.1 mm



(d)

0.1 mm



(e)

0.1 mm

Fig. 27. Titanium plate impacted at 775 K with an aluminum sphere (Shot 134): (a) crater cross section, (b) left side of crater, (c) crater bottom, (d) halfway between crater bottom and incipient spall, and (e) incipient spall zone.



(a)

1 mm



(b)



(c)

0.1 mm

Fig. 28. Titanium plate impacted at 775 K with a cadmium sphere (Shot No. 147): (a) crater cross section, (b) crater bottom, and (c) left side of crater.

in Fig. 27(e). In general, it is thought that the incipient spall condition did not have a significant effect on the crater dimensions partly because the backing plate prevented rear surface bulging of the target.

There was a significant difference between the morphology of the crater lips formed at room temperature and those formed at elevated temperatures. As can be seen by comparing Figs. 25 and 26 with Figs. 27 and 28, the craters formed at room temperature had almost no lip, while those formed at 775 K had a rather extensive lip. The details of a typically elevated temperature lip are illustrated in Fig. 29. This suggests that titanium has significantly more ductility under hypervelocity impact conditions at 775 K than at room temperature.

Clear dependency of crater parameters on projectile density was noted. It can be seen by comparing Figs. 25(a)-28(a) that the projectile density correlated with the smoothness of the crater. The craters made by the aluminum (Fig. 27) and glass (Fig. 25) projectiles were smooth, whereas those made by the denser materials, such as copper or cadmium, were rough on a scale of 0.5 mm (Figs. 26, 28, and 29). This effect appears to correlate with projectile density. Smoothness does not correlate with the shock state of the projectile, for of the four materials, only cadmium should vaporize. The roughness may be due to a Rayleigh-Taylor instability initiated by the pressure exerted by projectile material more dense than the target material.

Comparing the craters seen in Figs. 25-28 also illustrates a clear dependence of the crater depth-to-diameter ratio (p/D) with projectile density. It is clear from these photographs and from the data listed in Table II that the less dense projectiles produce craters with lower p/D than those made by the more dense projectiles. In fact, it appears from these data that all craters are generally ellipsoidal rather than hemispherical as is assumed in most penetration extrapolation equations.

Energy dispersive analysis x-ray (EDAX) scans were made of some targets to check that craters were actually formed by projectile materials. Both crater surfaces and polished cross sections were used. Trace amounts of silicon were always present, due perhaps to gun powder gases. Thus, glass could not be detected. Trace amounts of copper were found in the section from Shot No. 89. Copper-projectile-formed craters also usually appeared to have a copper tint inside. The EDAX detected copper on the surface of the crater produced

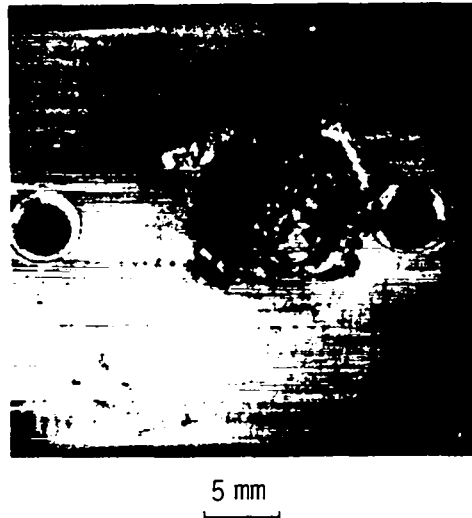


Fig. 29. Titanium plate impacted at 775 K with a copper sphere (Shot No. 133).

in Shot No. 141. In some cases, the copper was determined to have alloyed with the titanium target. Neither aluminum nor cadmium could be detected in the craters formed by these projectile materials.

It is clear from the photomicrographs of the impacted titanium that shock loading of this metal causes significant amounts of twinning (Figs 25-28). Twinned grains were found everywhere in the samples after impacting whereas there were none observed in the untested stock.

2. Titanium Alloys. One shot each was made into the titanium alloys Ti-5Al-2.5Sn and Ti-6242Si. Both targets were heated to 775 K. As can be seen in Fig. 30, both alloys are more impact resistant than pure titanium. In fact, the craters in both alloys made at 775 K appear very much like craters formed in pure titanium at room temperature.

A cross section of the crater in Ti-5Al-2.5Sn is seen in Fig. 31(a). The adiabatic shear zones in this alloy are almost as prominent as in pure titanium impacted at room temperature. The dark structure seen at higher magnification in Fig. 31(b) is probably indicative of a shock-induced phase transformation. Close examination of this phase reveals that it contains a very fine lamellar structure that is typical of a martensitic phase. As can be noted in Fig. 31(a), this phase appears to be precipitating along the adiabatic shear lines both under and around the crater. This would suggest that significant heat was generated locally causing a local temperature increase and, consequently, formation of some beta-titanium in the region. After

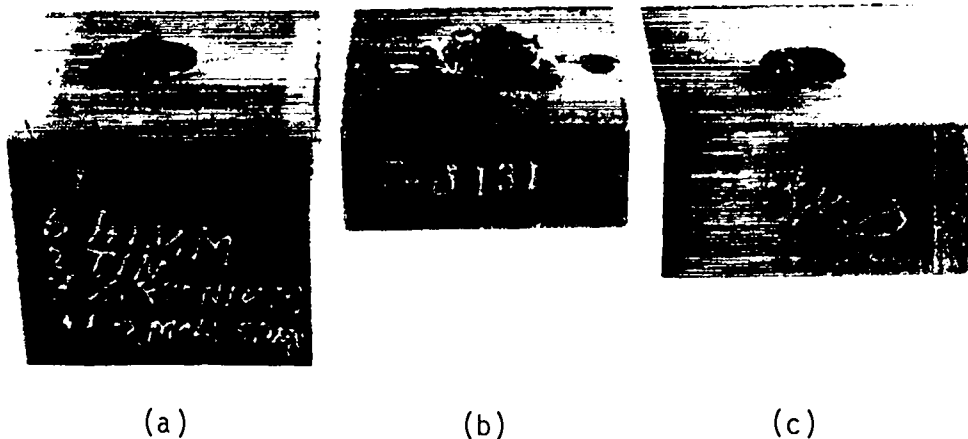
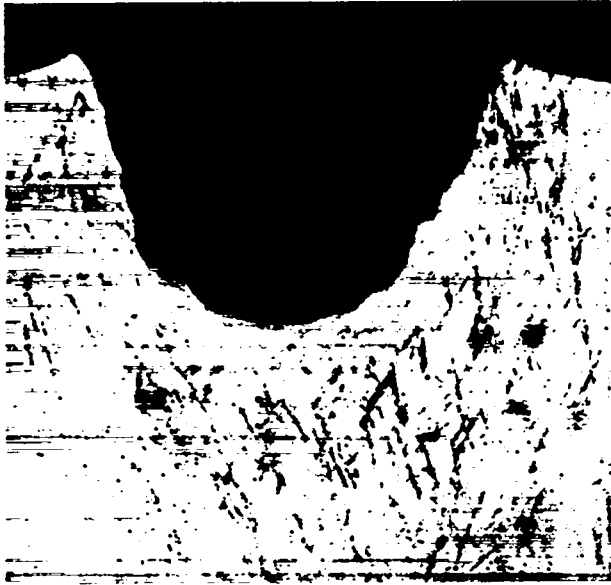


Fig. 30. Copper-projectile-produced craters in: (a) Ti-6242Si, (b) Grade 2 Ti (Shot No. 131), and (c) Ti-5Al-2.5Sn targets maintained at 775 K.

impact, these regions are quenched very rapidly causing martensite to form there. As can be seen in Figs. 31(c) and (d), the martensite did not form near the crater surface probably because the heating was more uniform in this area and cooling was slower. As with pure titanium, the copper-impact-formed crater in Ti-5Al-2.5Sn was very rough inside and, as can be seen in Fig. 32, had a checkerboard pattern on the bottom.

A cross section of the impact crater in Ti-6242Si is seen in Fig. 33(a). Adiabatic shear zones are visible in this photomicrograph and the one presented in Fig. 33(d). Due to the very fine grain structure, they are difficult to resolve. The scanning electron micrograph (SEM) of the crater bottom given in Fig. 33(b) illustrates both the magnitude and structure of the roughness inside the crater. The microstructure of the crater bottom is illustrated in the SEM given in Fig. 33(e). Both Figs. 33(c) and (d) illustrate the manner in which adiabatic shear zones interact with the crater surface. Both of these micrographs show evidence of shear displacements between blocks bounded by the adiabatic shear zones. In Fig. 33(d) we can see an open crack in the crater side wall. In addition, tiny dimples that are usually indicative of ductile failure of metals are seen in the SEM of the crater side wall seen in Fig. 33(c). This second feature appears to be an adiabatic shear zone that is intersecting the crater wall, because it tends to lie in a band.



(a)

1 mm



(b)

0.2 mm



(c)



(d)

Fig. 31. Ti-5Al-2.5Sn alloy impacted at 775 K with a copper sphere (Shot 151): (a) impact crater cross section, (b) crater lip, (c) crater bottom, and (d) crater side wall.

3. Beryllium. Two shots were made against beryllium targets with copper projectiles. One target was maintained at room temperature, Shot No. 159, while the second was heated to 775 K, Shot No. 160. Both targets behaved in a brittle manner that resulted in massive front surface spall and considerable secondary cracking. The general nature of the damage can be seen in Fig. 34. The details of the damage can be seen in the photomicrographs presented in Fig. 35. The cross-sectional view found in Fig. 35(a) shows the extent of the cracking that radiates from the impact crater. Some of these cracks can be seen intersecting with the crater bottom in the SEM in Fig. 35(b). As can be seen in Fig. 35(c), there was very little plastic flow under the crater bottom. The particle seen in the upper center of this photomicrograph on the crater bottom was determined, using EDAX, to be copper. The craters were so severely damaged in both targets that only their depths could be determined.

B. Thin Targets

The thin Grade 2 Ti targets were of three different configurations. Targets ranging in thickness from 2.54-8.25 mm were used to determine the proportionality between the TPT and the semi-infinite target crater depth.

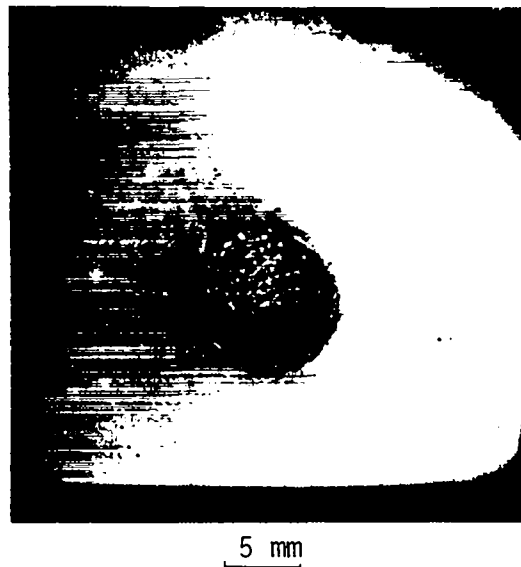


Fig. 32. Hypervelocity impact crater in Ti-5Al-2.5Sn, impacted with a copper sphere at 775 K.

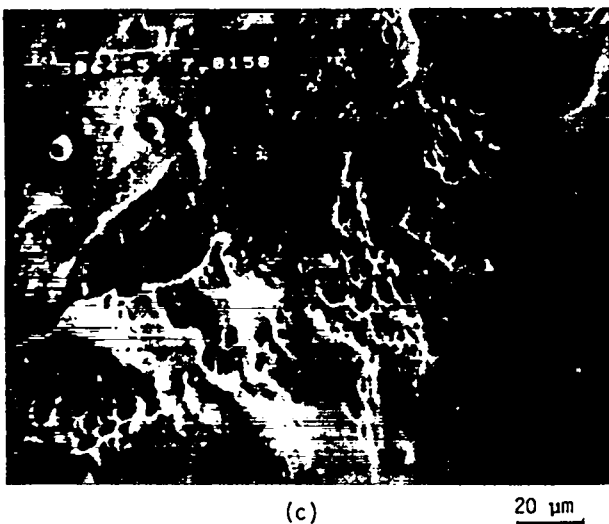
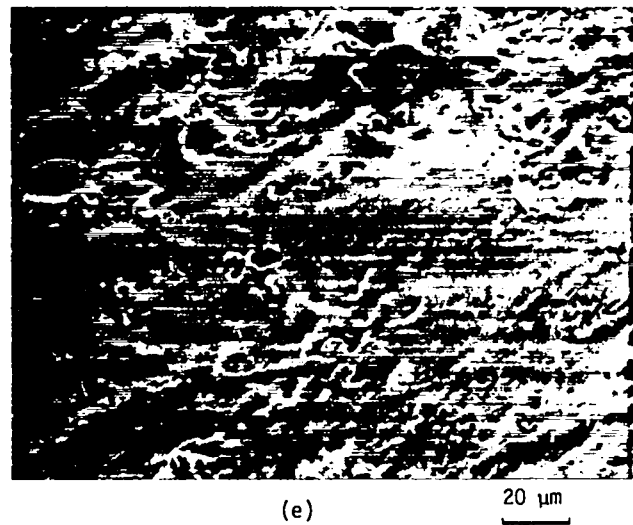
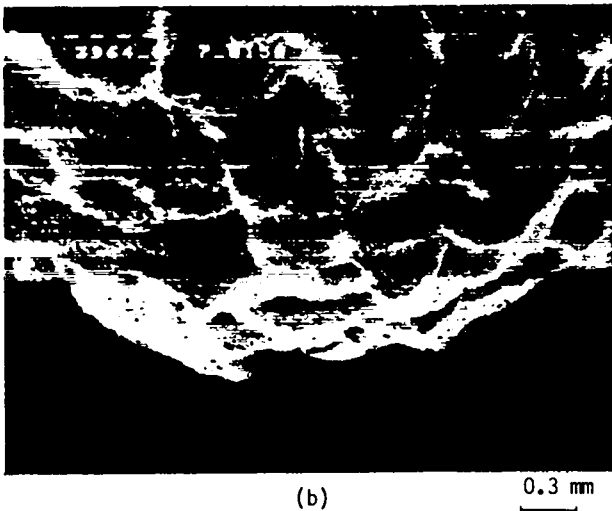
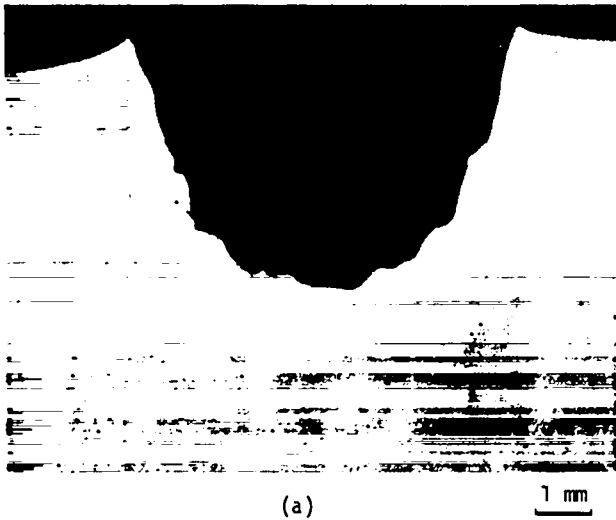


Fig. 33. Ti-6242 Si alloy impacted at 775 K with a copper sphere (Shot 150): (a) optical micrograph of crater, (b) SEM of crater bottom, (c) SEM, (d) optical micrograph of crater side wall, and (e) SEM of crater bottom surface.

The second set of targets, 0.66-mm-thick sheets, had one side shot-blasted with steel shot. The resultant roughened surface is a candidate distribution wick structure in the radiator heat pipes. The third set of targets were 0.55-mm Ti sheets coated with two different high emissivity coatings that included a white paint, zinc-orthotitanate, and a black coating, an amorphous carbon coating called D-111.

1. Threshold Penetration Thickness Targets. One target was impacted at room temperature, Shot No. 95. Figure 36 shows sequential frames from the B&W 300 high-speed camera for this shot. Here, the glass projectile can be seen approaching the target [Fig. 36(a)] followed by both backsplash formation and bulging of the back surface of the target [Fig. 36(b)]. In the final frame [Fig. 36(c)], a spall plate is seen to be in flight from the center of the bulge. The spall plate was measured to have been launched at a velocity of 213 m/s. This target appears to have been very close to TPT in this shot because it had a pinhole perforation after impact. The bulged and spalled back surface of this target is seen in Fig. 37. The impact parameters and results for this and other shots in this series are listed in Table II.

A total of six shots were made into titanium targets heated to 775 K to determine their TPT. Two impacts were made with 1.59-mm-diam copper projectiles, and four were made with 1.4-mm-diam glass beads. In one of the



Fig. 34. Beryllium target impacted with a copper sphere at room temperature (Shot No. 159).

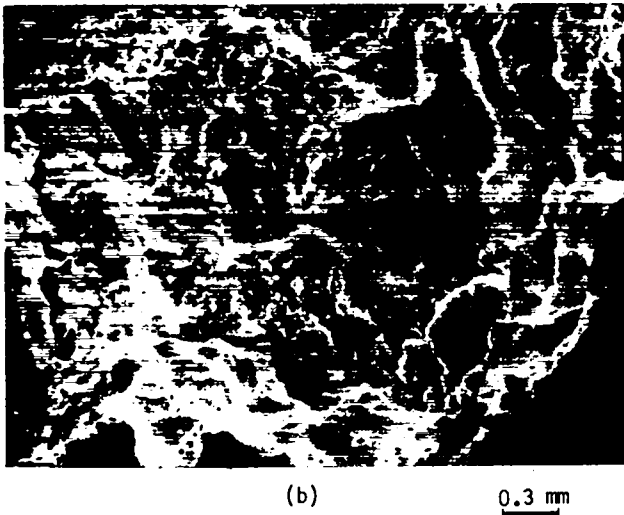
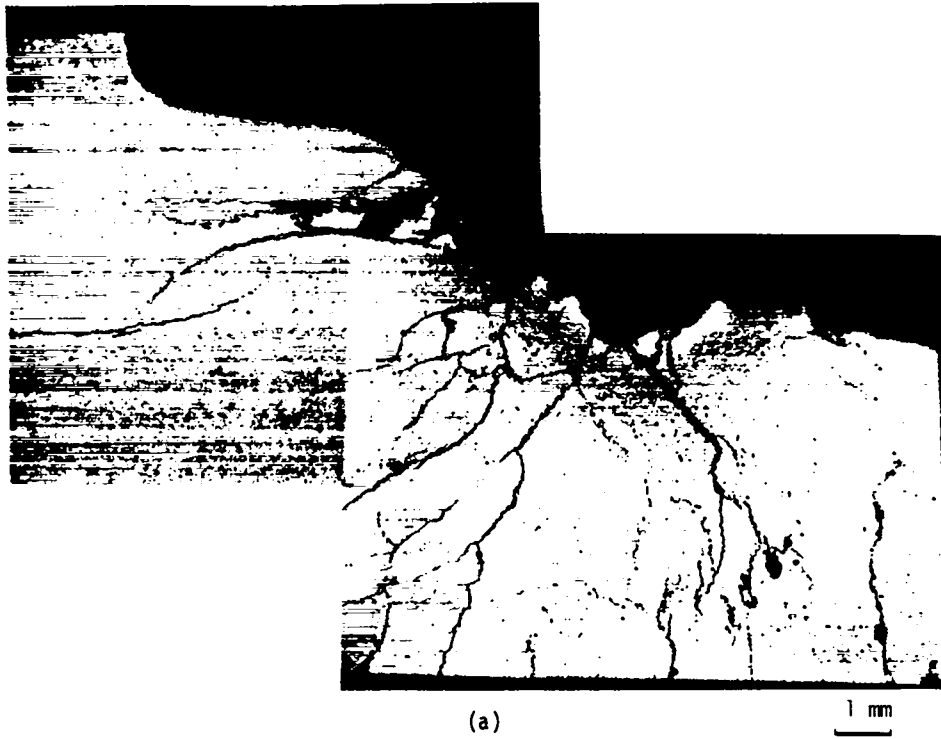
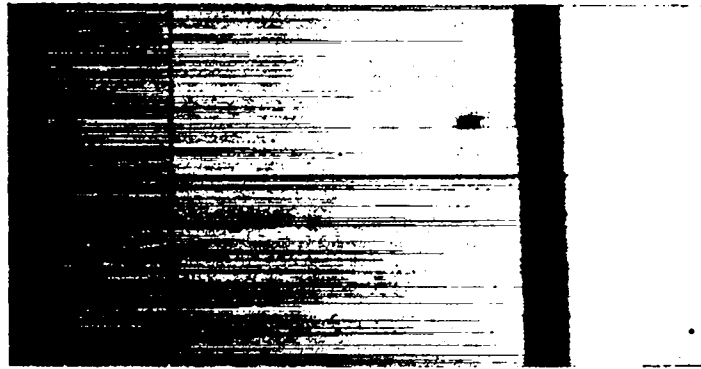
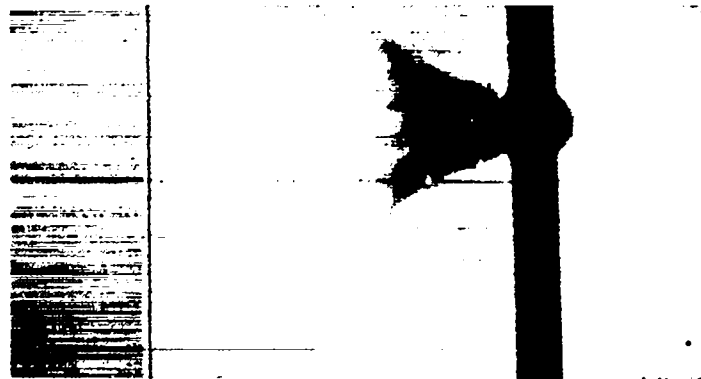


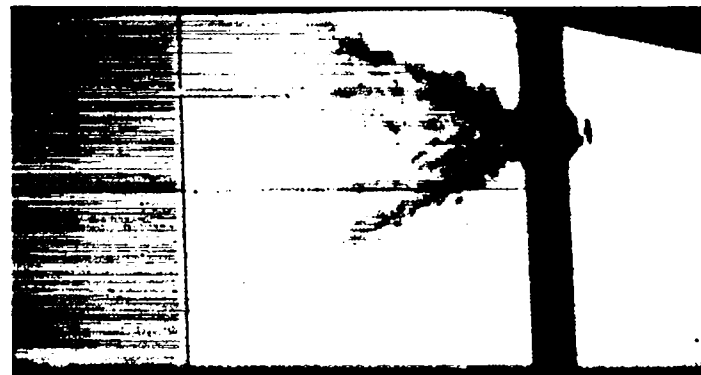
Fig. 35. Beryllium impacted with a copper sphere at room temperature (Shot No. 159): (a) crater cross section, (b) SEM, and (c) optical micrographs of crater bottom.



(a)



(b)



(c)

Fig. 36. Photograph sequence made with the B&W 300 high-speed camera, from Shot No. 95: (a) 1-mm-glass bead in flight at 6.12 km/s, (b) bead has impacted on 2.78-mm-thick Grade 2 Ti target, and (c) spall break-out of back side of target.

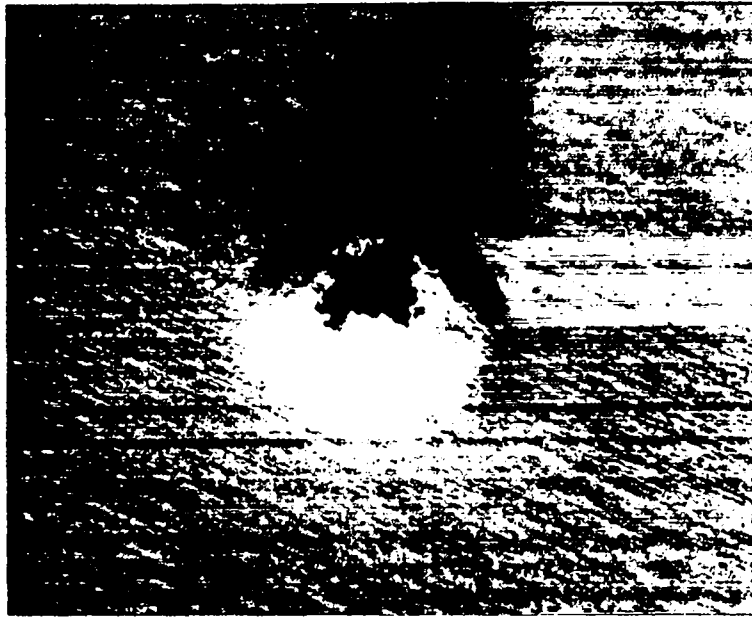
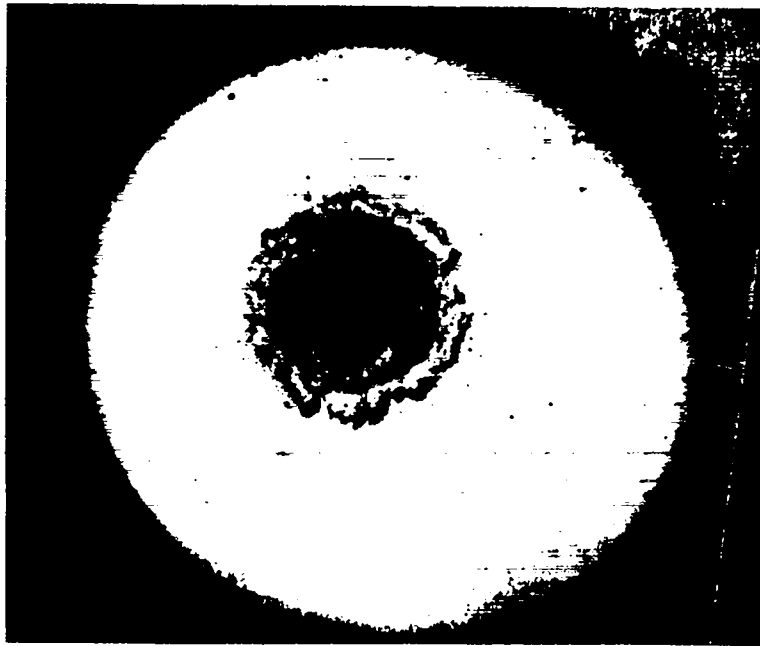


Fig. 37. Rear surface from Shot No. 95, showing where spall was ejected.

experiments, a glass bead was impacted into the surface of the target at an angle of 45° to study the effects of obliquity on TPT.

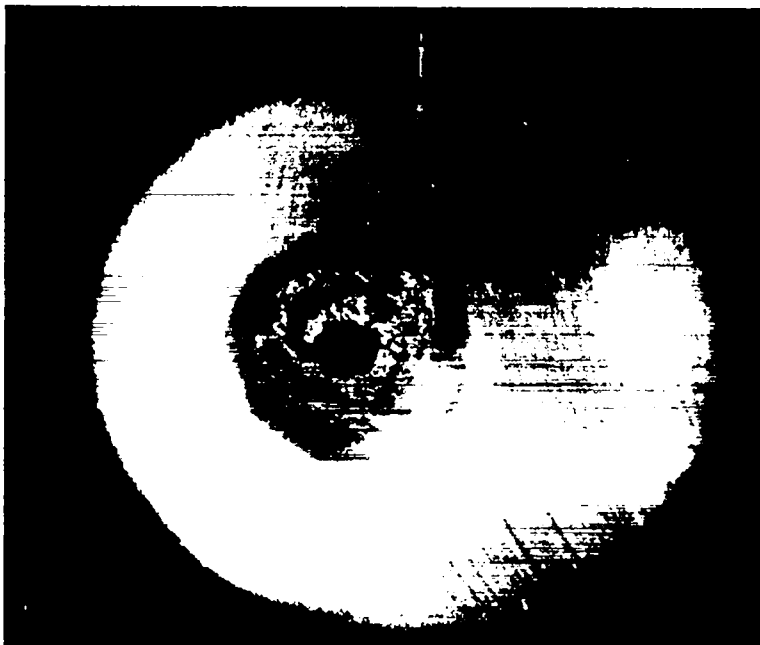
Assuming the $TPT = 1.5 p$ and calculating p from the C-S equation, it was estimated that the target in Shot No. 141 that was impacted with a copper projectile should have been just perforated. However (Fig. 38), the perforation does not appear to be near a threshold level. The crater formed in this shot looks very much like those formed in the thick targets. It was also estimated that the target in Shot No. 137 that was impacted with a glass projectile should have been very close to threshold penetration, and in fact it was. This can be clearly seen in Fig. 39, especially Fig. 39(c), which illustrates just how close the target was to perforation.

The results from Shot No. 142 are in doubt. The crater from this shot is definitely shallower than usual. It also has an anomalously small diameter. The mean crater diameter for all other shots into heated titanium with 1.44-mm beads was 5.68 mm with a standard deviation of 0.44 mm. There is a slight velocity dependence, but the mean includes data from shots at lower velocity than Shot No. 142. The diameter of the crater in Shot No. 142 is only 4.2 mm. Thus, it is probable that the datum from 142 is spurious--the crater may be due to a sabot fragment.



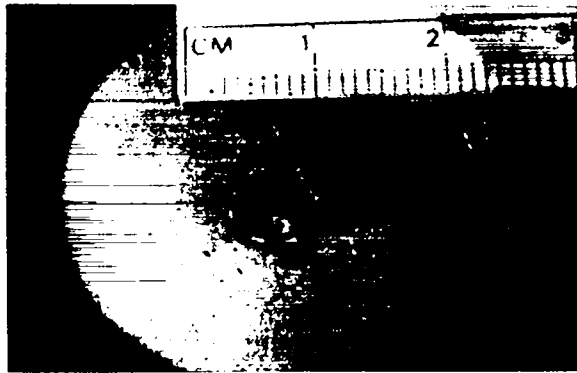
(a)

5 mm

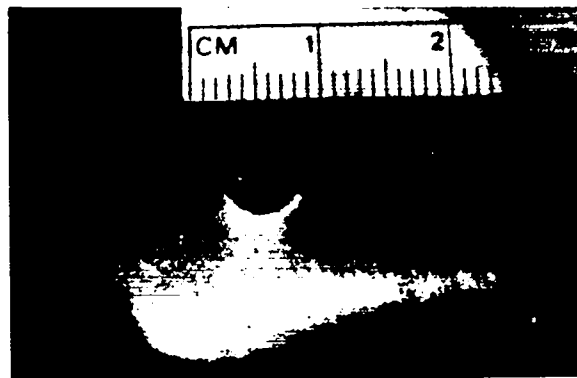


(b)

Fig. 38. Titanium plate impacted at 775 K with a copper sphere (Shot No. 141): (a) impact crater on front surface and (b) bulged and spalled rear surface.



(a)



(b)



(c)

Fig. 39. Titanium plate impacted at 775 K with a glass bead (Shot No. 137):
(a) impact crater on front side, (b) bulged and spalled rear surface, and (c) crater cross section.

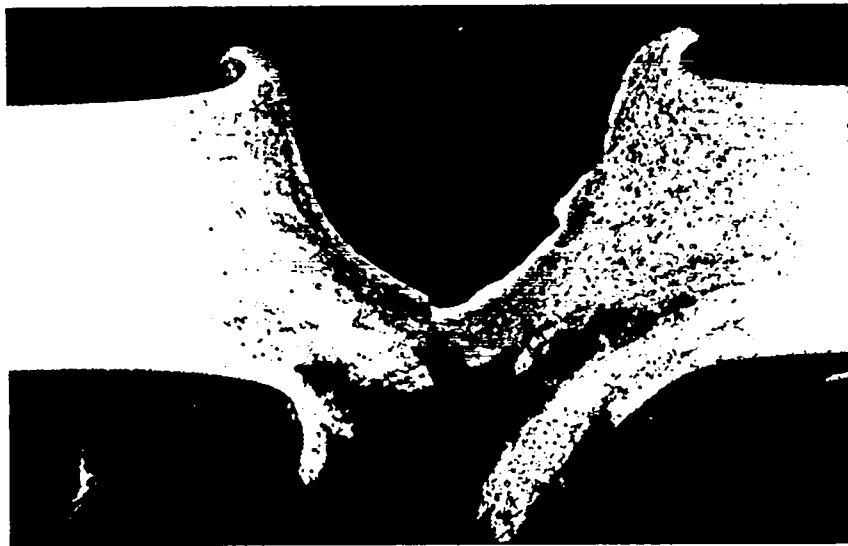
Shot No. 143 was conducted with an impact angle of 45° using a glass bead. As seen in Fig. 40(a), the impact crater is nearly symmetric, but comparing this shot with the nearly identical Shot No. 137 reveals a definite skew in the spalling pattern that appears to have been caused by the angle of impact. Perforation for this shot is shown in detail in Fig. 40(b). As can be seen in Figs. 40(a) and 40(c), adiabatic shear zones appear only on the side of the crater normal to the projectile trajectory.

2. Shot-Blasted and Coated Targets. Four shots were conducted against targets containing thin plates which had an emissivity coating or shot peening to simulate surfaces proposed for the space radiator. The details of the tests and their results are summarized in Table III.

In Shot No. 152, a 0.66-mm-thick, shot-blasted sheet was bonded to a 3.22-mm Grade 2 Ti substrate. It was struck with a 1.4-mm-diam bead. The front plate spalled off. A partially detached spall plate emitted from the rear surface of the support plate. The perforation was consistent with that of monolithic targets. No anomalies associated with the shot peening were observed.

Emissivity coatings were tested in Shot Nos. 154 and 156. A 0.5-mm coated sheet was bonded to a 9.5-mm-thick sub-block in each case. The surface plate was always spalled off the sub-block around the crater in a region about 2-3 crater diameters wide. Total penetration was 2.15 and 2.29 mm. The predicted value, using the C-S equation and $K_0 = 1.5$, is 5.62 mm. The great reduction in crater depth must be associated with the surface plate, although it is difficult to understand how the coating per se could have influenced the event. One possibility is that while hot, the bond loosened, so that the plate provided a "bumper" effect, shattering the projectile just before it hit the main target block.

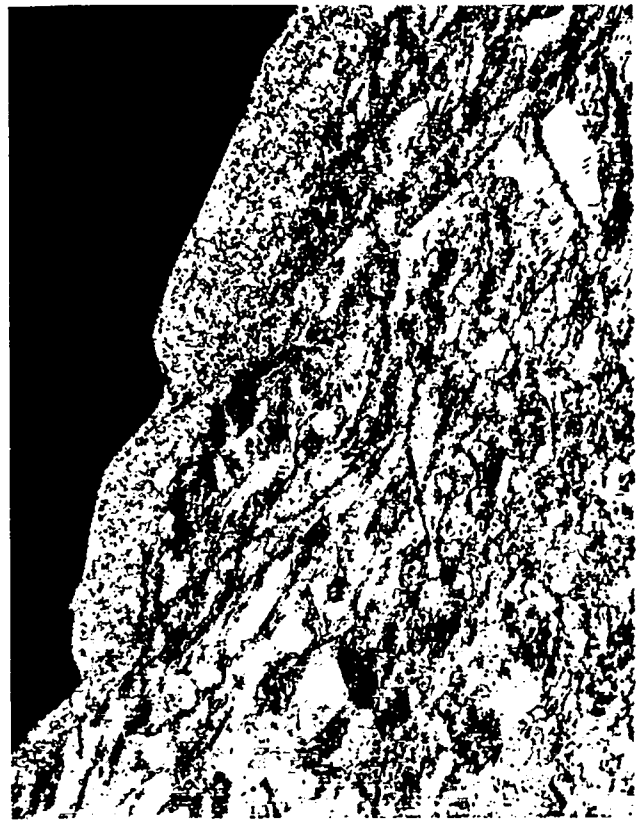
In order to eliminate problems with sandwich targets, it was decided to perforate a 0.56-mm-thick shot-blasted titanium sheet with a 0.5-mm bead, and examine the resulting targets for anomalies traceable to surface treatment. The peened surface was the rear surface. Figure 41 is a photomicrograph of the target (Shot No. 158). The spall cap did not lift in a dome away from the perforation, as is usually observed. Rather, there was a tendency to peel back the shot-peened surface. Shot peening tends to slightly reduce spall. Thus, designs evolved from data for non-shot-peened targets will not be jeopardized



(a)



(b)



(c)

Fig. 40. Titanium plate impacted at 775 K with a glass sphere (Shot No. 143) at 45°. (a) perforated crater, (b) crater bottom, and (c) crater side.

TABLE III
SHOT-BLASTED AND COATED TARGET DATA

Target Description	Target Thickness (mm)	Temp. (K)	Shot No.	d (mm)	u (km/s)	Results
0.66-mm shot-blasted Ti, bonded to 3.22-mm Grade 2 Ti	3.96 total	775	152	1.4	6.0	spalled off surface plate spalled rear of backplate
Zincorthotitanate coated Ti .55 mm, bonded to 9.5-mm substrate	10.2 total	295	154	1.4	6.59	2.15-mm total penetration
0-111 emissivity coating Ti .56 mm bonded to Ti substrate 9.5 mm	10.2 total	295	156	1.4	6.60	p = 2.29 mm total
Shot-blasted Grade 2 Ti	0.56	295	158	0.5	7.17	perforation 1.5 mm diameter

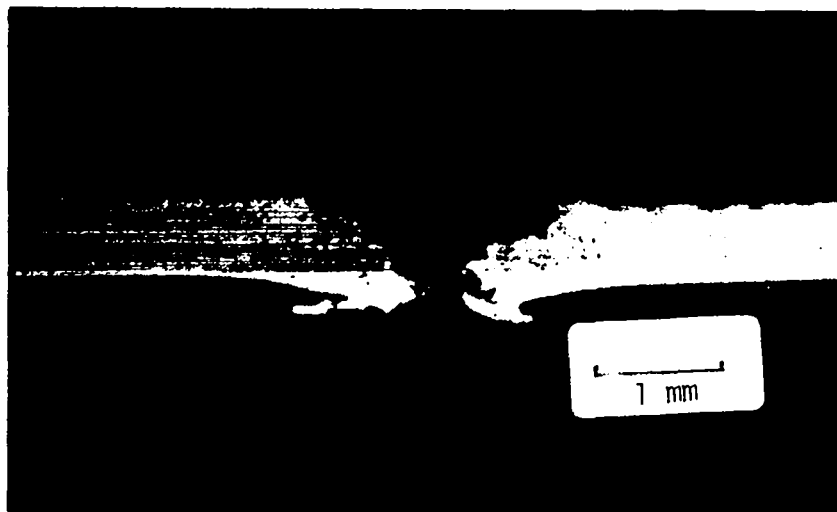


Fig. 41. Photomicrograph of target from Shot No. 158: 0.66-mm-thick, shot-peened titanium plate struck by 0.5-mm bead.

when shot-peened plates are used. These results could be more firmly established by either impacting non-shot peened 0.66-mm plate with 0.5-mm glass beads at exactly the same velocity as Shot No. 158 or by doing an exact size scale-up. Either of these approaches would probably have involved a substantial number of shots, and it was felt that the cost would be excessive for the benefit.

V. DATA ANALYSIS

As mentioned earlier, the experimental, hypervelocity impact data has to be fitted to some extrapolation model, such as the C-S equation, to predict meteoroid resistance of the hardware in question. The thin-target data were compared with the thick-target data to attempt a determination of the correlation between TPT and crater depth in semi-infinite targets.

A. Thick Targets

1. Grade 2 Titanium. Table IV presents the calculated values of the C-S material parameter, $S_t^{1/3}$, and the cratering efficiency, $\epsilon^{1/3}$. In computing S_t for glass spheres, density is the most uncertain parameter, so the rearranged C-S equation,

$$S_t = \frac{3^5 m^2 u^2}{4\pi^2 \rho_t d^3 p^3} \quad , \quad (8)$$

was used, whereas for the copper, aluminum, and cadmium projectiles, projectile density was accurately known and it was more exact to calculate S_t from

$$S_t = \frac{3^4 \rho_p m u^2}{8\pi \rho_t p^3} \quad . \quad (9)$$

The best values of $S_t^{1/3}$ and $\epsilon^{1/3}$ for various impacts have been calculated from the data in Table IV by using inverse variance weighting. The results for room temperature are $S_t^{1/3} = 3.82 \text{ (GJ/m}^3)^{1/3}$ and $\epsilon_t^{1/3} = 1.57 \text{ (GJ/m}^3)^{1/3}$. (This calculation did not include Bruce's^a Grade 4 Ti value for $S_t^{1/3}$ of $3.85 \text{ (GJ/m}^3)^{1/3}$.) The relative standard deviations are 8 and 6.5%, respectively. If the variations from shot to shot are interpreted as statistical and due to measurement error, then we would be justified in calculating the uncertainty in mean values by dividing the standard deviation by $\sqrt{N-1}$. However, if they are considered truly representative of the intrinsic variability of the cratering process, then the full standard deviation should be retained. In fact, both sources contribute to the variation. For design purposes, prudence commends using the larger uncertainty value. Thus, we conclude that for room temperature, Grade 2 Ti:

^aThis information provided by E. Bruce, The General Electric Co.

TABLE IV
SUMMARY OF THICK-TARGET CRATER DATA

Target	Proj.	Shot No.	E (J)	p (mm)	v (mm ³)	S _t ^{1/3} (GJ/m ³) ^{1/3}	ε ^{1/3} (GJ/m ³) ^{1/3}
Grade 2 Ti 295 K nom.	G	82	4.39 ± .28	0.80	1.13	3.65 ± .25	1.57 ± .07
	G	90	21.8 ± .6	1.36	3.66	3.74 ± .12	1.81 ± .05
	G	84	46.2 ± 1.7	1.70	11.92	3.85 ± .13	1.57 ± .03
	G	96	118.4 ± 1.9	1.87	22.3	4.31 ± .06	1.74 ± .06
	G	105	161.5 ± .9	2.42	34.5	4.03 ± .04	1.56 ± .05
	Cu	94 ^a	323 ± 9	4.66	93.7	3.43 ± .06	1.51 ± .02
	Cu	88	334 ± 7	4.72	85.1	3.43 ± .02	1.58 ± .02
	Cu	89	350 ± 5	4.54	95.3	3.62 ± .14	1.54 ± .02
Grade 2 Ti 775 K nom.	G	99	108.4 ± 5.3	2.64	40	3.23 ± .09	1.39 ± .18
	G	104	139.2 ± .8	2.90	55.3	3.20 ± .06	1.36 ± .03
	Cd	147	397 ± 7	5.26	130	3.22 ± .03	1.45 ± .03
	Cu	130	473 ± 7	5.43	163	3.34 ± .06	1.43 ± .02
	Cu	133	531 ± 4	5.17	185	3.65 ± .03	1.42 ± .02
	Al	134	571 ± 10	4.17	156	3.11 ± .02	1.54 ± .05
	Cu	131	588 ± 8	6.38	205	3.06 ± .02	1.42 ± .04
	Cu	132	627 ± 4	6.22	120	3.21 ± .02	1.74 ± .03
	Ti-5Al-2.5Sn 775 K	Cu	150	534 ± 5	4.53	110	4.17 ± .03
Ti-6242Si 775 K	Cu	151	464 ± 4	4.53	121	3.99 ± .03	1.56 ± .03
Be, 295 K	Cu	159	556 ± 8	5.64	NA	4.59 ± .09	NA
Be, 775 K	Cu	160	514 ± 8	6.94	NA	3.64 ± .08	NA

^aThis target was heated to 475 K.

$$S_t^{1/3} = 3.82 \pm 0.31 \text{ (GJ/m}^3\text{)}^{1/3} ,$$

$$\epsilon^{1/3} = 1.57 \pm 0.10 \text{ (GJ/m}^3\text{)}^{1/3} .$$

For Grade 2 Ti heated to 775 K, the corresponding values are

$$S_t^{1/3} = 3.20 \pm 0.18 \text{ (GJ/m}^3\text{)}^{1/3} ,$$

$$\epsilon^{1/3} = 1.46 \pm 0.12 \text{ (GJ/m}^3\text{)}^{1/3} .$$

It is surprising how consistent those values of $S_t^{1/3}$ and $\epsilon^{1/3}$ are. The variation in these parameters is proportional to the uncertainty in predicted penetration depth. For all the values above, the mean relative uncertainty is only 7%. This is remarkably small considering the large span of projectile energy and density encompassed by the data.

The fit of the crater volume data to a proportionality relationship with the projectile kinetic energy is shown graphically for room temperature and 775 K Grade 2 Ti in Fig. 42. The fit appears reasonably good, and the small reduction in the value of the cratering efficiency with increasing temperature is illustrated in this figure.

The good fit of the titanium penetration data to the C-S equation is seen in Fig. 43. This plot also illustrates the very small effect of temperature on the penetration behavior of Grade 2 Ti.

The variation of $S_t^{1/3}$ with projectile density is shown in Fig. 44. For hot targets, $S_t^{1/3}$ appears to increase slightly with density, while

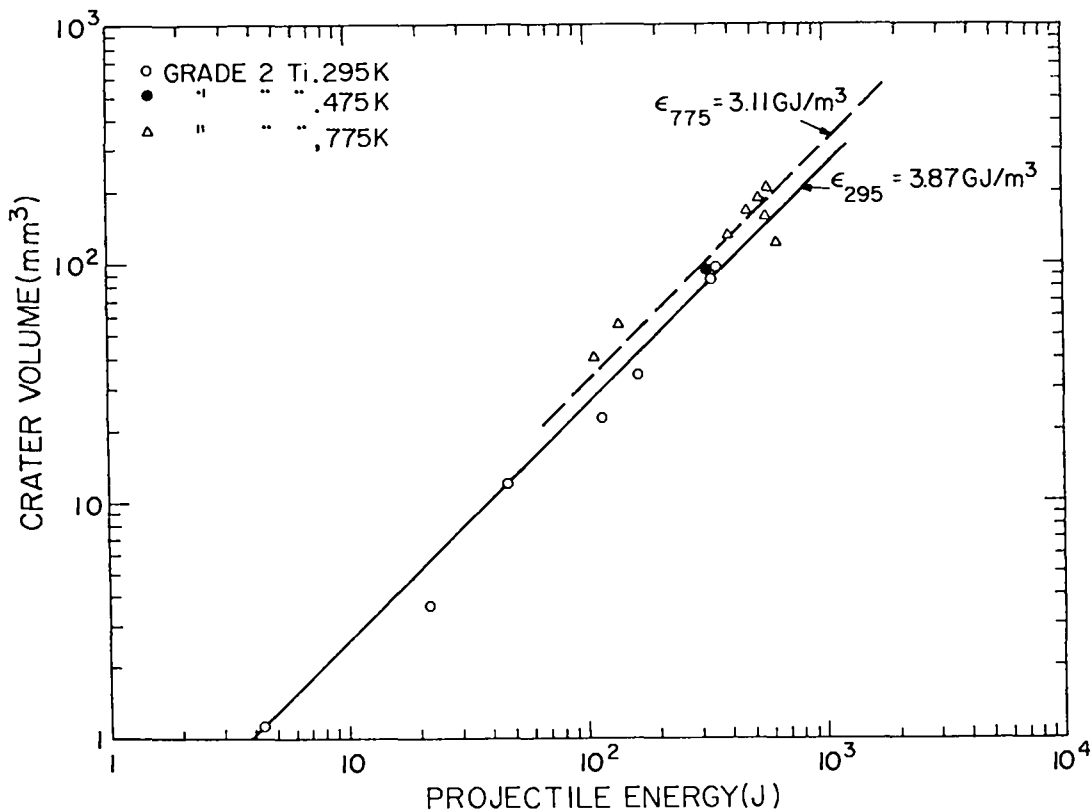


Fig. 42. Crater volume data for thick titanium targets fitted to $V = E/\epsilon$.

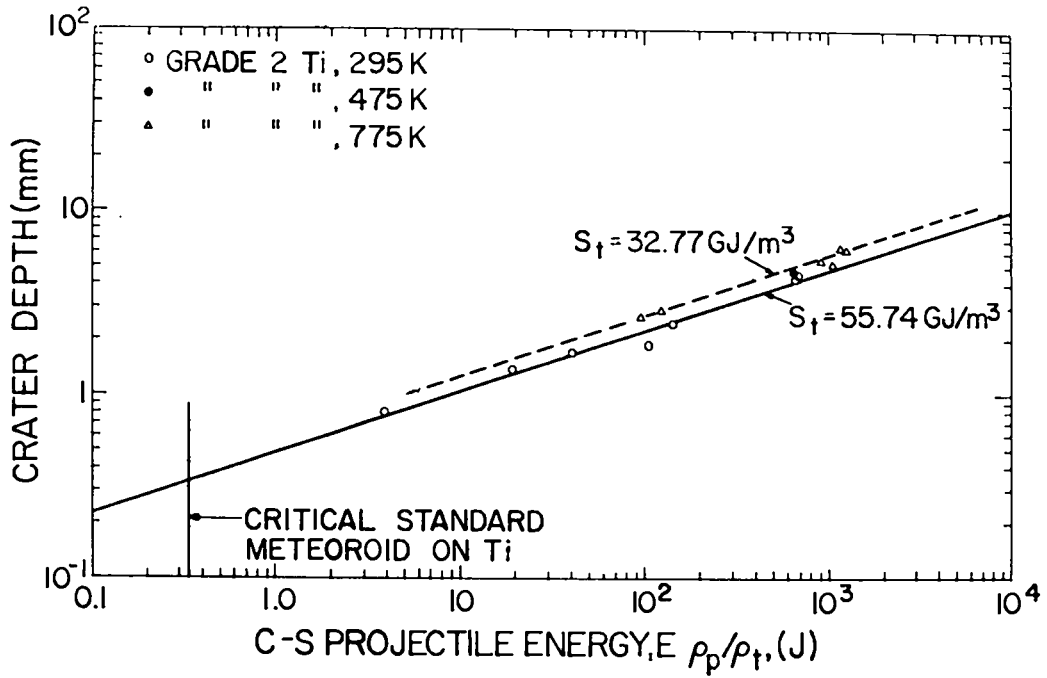


Fig. 43. Crater depth data for thick titanium targets fitted to C-S equation.

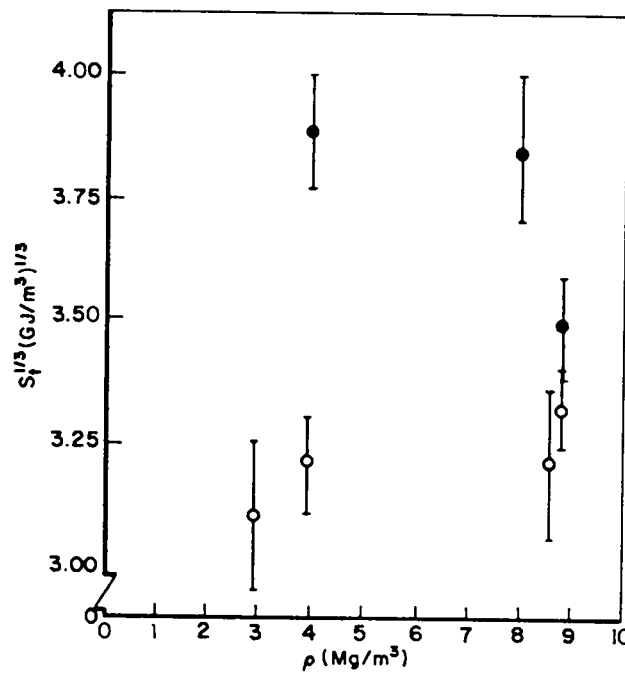


Fig. 44. Dependence of C-S penetration parameter on projectile density for titanium. Open circles, 775 K targets; closed circles, 295 K.

for cold targets, it appears to decrease slightly. Because of these contradictory results, it is probably not warranted to adjust the density dependence of the C-S equation away from that indicated in Eq. (3).

The variation of $\epsilon^{1/3}$ with projectile density is shown graphically in Fig. 45. As can be seen, there appears to be no statistically supported density dependence for the cratering efficiency.

2. Titanium Alloys. As noted in Table IV, both titanium alloys were significantly more impact resistant than pure titanium. The C-S energy parameter is about 30% higher for Ti-5Al-2.5Sn and about 25% higher for Ti-6242Si. There is a lesser improvement in the volume parameter.

3. Beryllium. The $S_t^{1/3}$ parameter for hot beryllium was $3.65 \text{ (GJ/m}^3)^{1/3}$. Because TPT is proportional to $(\rho_t S_t)^{1/3}$, it is 29% greater for a beryllium plate than for a titanium plate. In terms of weight, a beryllium plate giving the same protection as a titanium plate weighs only half as much as the titanium plate. However, for most applications, the brittleness of the beryllium would probably render it unsuitable.

A value of $\epsilon^{1/3}$ was computed for beryllium from the values for $S_t^{1/3}$ by fixing $p/D = 0.5$ (hemispherical craters). The results were 1.14 and 0.9 $(\text{GJ/m}^3)^{1/3}$ for 20°C and 500°C material, respectively.

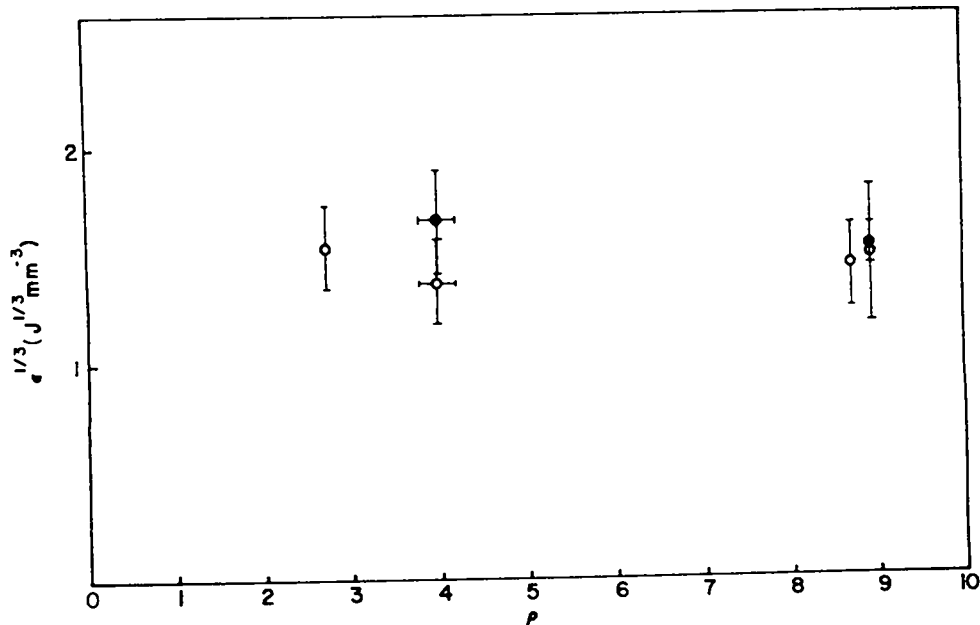


Fig. 45. Dependence of cratering coefficient on projectile density for titanium. Open circles, 775 K targets; closed circles 295 K.

The temperature of beryllium seems to strongly affect $S_t^{1/3}$. Combining these results with those of Diedrich, et al.⁸, one obtains

T(K)	$S_t^{1/3}(\text{GJ/m}^3)^{1/3}$
295	4.59 ± 0.09
775	3.64 ± 0.08
980	3.35 ± 0.20

B. Threshold Penetration vs Crater Depth for Titanium

The thin-plate data are compared to calculated semi-infinite target penetration for the same impact condition, and as can be seen in Table V the values of t^*/p are sometimes greater than 1.5 when titanium perforates using the C-S equation to calculate the semi-infinite target penetration. If one

TABLE V
THIN-TARGET RESULTS OBTAINED IN THIS STUDY FOR
GRADE 2 Ti at 775 K

Shot No.	Parallel Target Thickness ^b , t^* (mm)	t^*/p_{C-S}	RESULTS
95 ^a	2.54	1.57	Pinhole perforation
136	7.24	1.33	Perforation
137	3.94	1.52	Spall, no perforation
141	8.25	1.46	Perforation
143	4.59	2.14	Perforation, symmetric crater
($\alpha = 45^\circ$)			
144	3.56	~1.27	Perforation and spall

^aThis target was maintained at room temperature while others listed in this table were heated to 775 K before impact.

^bThe thickness of the target parallel to projectile flight direction, $t^* = t/\sin \alpha$, where α is the angle between the target surface and the flight trajectory.

examines the results from this study and from Bruce's work⁹ listed in Table VI, it appears that oblique impacts causing perforation have a much higher t^*/p value than the normal impacts that cause perforation. These data would suggest that the K_0 factor is greater than 2.1 for Grade 2 Ti at 775 K with an impact angle of 45° , while for Grade 4 Ti at room temperature with impact angles at 10° or less, it appears to run higher than 2.2 times the penetration depth calculated with the C-S equation.

It is clear that we have not uniquely determined K_0 for titanium from these data.

VI. DISCUSSION

A. Material Behavior

1. Titanium and Titanium Alloys. As we have shown, there is little effect of either temperature or alloy strength on the hypervelocity impact resistance of titanium and its alloys. This is true even when we compare the results of this study with the published data^{7,9}. Combining all of the data, we see a strong indication that there is an impact angle effect on the perforation resistance of titanium; however, there is insufficient data to quantify the effect. The surface condition variations studied also do not seem to have any significant effect on the impact resistance of titanium.

TABLE VI
THIN TARGET OBLIQUE IMPACT RESULTS OBTAINED BY BRUCE⁹ FOR
GRADE 4 Ti AT ROOM TEMPERATURE

Projectile (302 SS Spheres) Diameter (mm)	Velocity (km/s)	Parameters Angle, α^a ($^\circ$)	Parallel Target Thickness, t^* (mm)	t^*/p_{C-S}^b	Results
3.18	7.25	10	6.00	0.68	Perforation
3.18	7.38	8	7.48	0.84	Perforation
3.18	7.76	3	19.90	2.16	Perforation
3.18	6.53	10	21.21	2.59	No Perforation
1.59	7.19	5	11.95	2.72	No perforation
3.19	6.08	2	29.83	3.78	No perforation

^aSee footnote b, Table V.

^bSemi-infinite target penetration depths, p_{C-S} , were calculated using the Grade 2 Ti material determined in this study.

The adiabatic shear phenomenon that was observed in pure titanium and both of the titanium alloys studied has been observed previously.¹⁰ Especially in Figs. 25 and 26, there is clear evidence of relative shear displacement across the adiabatic shear zones. The impurity stringers are seen to be displaced laterally across the shear zones. It is also clear in these two figures that this localized shearing process can eventually lead to fracture. The voids like those found by Winter¹⁰ in rapidly deformed titanium appear to have coalesced to form cracks at both the bottom and side of the craters formed in the titanium in this study. However, the cracks in room temperature titanium appear to have a periodic nature in general. The shear bands formed in titanium at elevated temperatures are much less pronounced (Fig. 27), but they are still present.

It is suspected that the adiabatic shear bands in both titanium and Ti-5Al-2.5Sn are the transformed type described by Rogers¹¹, that is, the deformation heat caused the metal in the shear zone to be raised above the alpha-beta transformation temperature, and when the zone was quenched after impact, a martensitic structure was produced. It is interesting to note that the Ti-5Al-2.5Sn alloy transformed along the shear lines at considerable distance from the impact crater (Fig. 31). The shear traces delineated in this alloy and in pure titanium (Figs. 25 and 26) are significantly distorted from the theoretical pattern given by Backman and Finnegan¹². The diamond pattern observed beneath the crater is much flatter than their theoretical pattern, and the observed sidewall shear bands enter the crater at a much steeper angle than predicted.

It is suspected that adiabatic shear plays a major role in titanium perforation when the impact is significantly off-normal in orientation. If one compares the details of the perforation morphology in Fig. 40(a) with the adiabatic shear zone pattern that is especially well delineated in Fig. 31(a), he will note that there is a striking similarity of their geometries. It appears that the perforated sample (Fig. 40) failed on intersecting adiabatic shear zones.

The indication that the propensity toward adiabatic shear significantly affects the impact resistance of titanium and its alloys creates great incentive to study the relationship further. Both experiments and computer simulations need to be performed. These further studies should also include a

precise determination of the relationship between threshold penetration and semi-infinite target impact crater depth in these materials.

2. Beryllium. The hypervelocity impact behavior of the beryllium tested is sufficiently poor to render it impractical for an application such as a space radiator heat pipe. The brittleness of this metal would probably cause a heat pipe impacted with the smallest meteoroid to leak through secondary cracks like those seen in Fig. 35. Open cracks would lead to heat pipe failure.

The beryllium impact behavior noted in this study is essentially no different from that observed by Diedrich, et al.⁸ They reported significant secondary cracking in beryllium impacted at both room temperature and 980 K. Beryllium might be useful as an armoring material if it could be backed with a ductile support material that could arrest cracks propagating through the beryllium after impact.

B. Implications for Radiator Design

Because the radiator surface is composed of many heat pipes, the radiator area is effectively segmented into many individual, independent units. This system of individual heat pipes must be designed to absorb a predictable number of losses and function at full heat-rejection capacity for the duration of the entire system mission. Of course, the radiator must have a minimum mass consistent with this goal. Table VII contains a list of the basic design criteria to be satisfied by the radiator used in the SPAR system. With the aid of the NASA near-Earth meteoroid environment model and the Poisson distribution equation [Eq. (3)] described earlier, the probability of impact by n particles of mass m or greater can be established. Because impacts by particles of mass m or greater will penetrate the armor protection of the heat pipes, the radiator may lose n heat pipes due to meteoroid impact. If the heat pipes can withstand the impacts of smaller meteoroids, then the Poisson distribution probability,

TABLE VII
RADIATOR DESIGN CRITERIA

Radiator Power (kW)	1010
Operating Temperature (K)	775
Mission Duration (yr)	7
Radiator Survival Probability	0.99

$P_{x < n}$, becomes the radiator survival probability, and the number of heat pipes surviving the mission can be predicted. With this information, a minimum-weight heat pipe can be designed so that the surviving heat pipes can adequately reject the waste heat.

Of primary concern, therefore, is the optimization of the number of radiator heat pipes required to provide adequate system redundancy to absorb some losses due to meteoroid impact. Another dimension of the optimization is the selection of the maximum mass meteoroid to defend against. This latter aspect is derived from a material penetration equation such as the C-S equation [Eq.(4)]. For purposes of radiator design, this equation was used in sensitivity studies of titanium radiator mass vs critical meteoroid mass and the number of heat pipes. Plots of radiator mass vs meteoroid mass calculated from the C-S equation are presented in Fig. 46 for a K_0 value of 1.5.

As can be seen in Fig. 46, the titanium radiator masses are minimized for meteoroid masses in the range 1.25×10^{-5} to 1.75×10^{-5} g using either 270 or 360 heat pipes. Increases in the radiator masses to the left of the

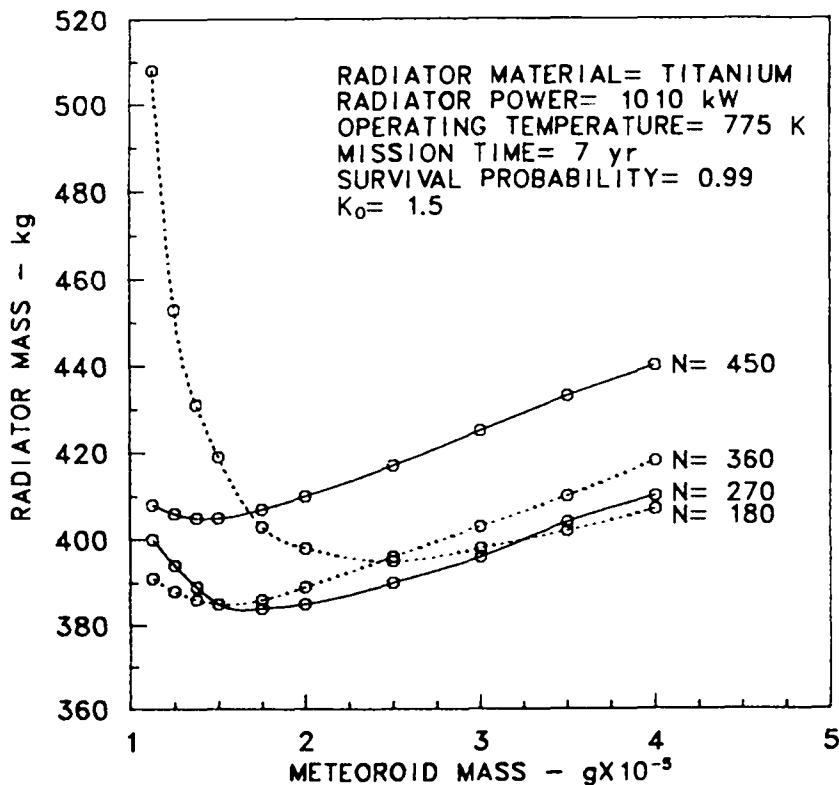


Fig. 46. Radiator mass vs meteoroid mass for armor thicknesses calculated with the C-S equation.

minima are due to increases in the number of impact losses that must be absorbed, while increases in radiator masses to the right of the minima are due to increased armor thickness.

From the radiator mass minimization plots in Fig. 46, we estimate a critical standard meteoroid has a mass of 1.5×10^{-5} g. The kinetic energy of this particle is 3J which is slightly below the energy range of particles launched in this study. Also, as indicated in Fig. 43, the C-S energy-density parameter E_p/ρ_t , for the critical standard meteoroid impacting titanium is about an order of magnitude below that for the least energetic particle launched in this study. This means that penetration predictions based on the C-S equation require a greater extrapolation than those based on the energy-volume relation, Eq. (5).

Using $K_0 = 1.5$ and the C-S equation for calculating the armor thickness required to protect against a critical standard meteoroid, we find the required thickness is 0.6 mm. However, if we use the crater volume/meteoroid energy relationship determined in this study with $K_0 = 1.5$ and assume the formation of hemispherical crater, we calculate the armor thickness should be 1.16 mm.

VII. CONCLUSIONS AND RECOMMENDATIONS

This study has gone far to define the hypervelocity impact behavior of titanium, titanium alloys, and beryllium. The cratering behavior of these materials has been quantified; however, the correlation between semi-infinite target cratering and thin target perforation needs better definition. More experiments are required in this area with more emphasis being given to oblique impacts. This study indicated that target temperature had little effect on the hypervelocity impact behavior of titanium, but there was a strong effect on the impact behavior of beryllium. The high-temperature titanium alloys, Ti-5Al-2.5Sn and Ti-6242 Si, were found to have better impact resistance than commercial-pure, Grade 2 Ti. The tendency toward adiabatic shear in titanium appears to influence its perforation behavior such that the value of the ratio of the target perforation the thickness to the semi-infinite target penetration depth, K_0 , appears to be higher for this material than for most.

Beryllium was found to behave in a manner that is unacceptable for heat pipe radiator applications. That is, its brittle behavior would cause heat pipe failure to occur by secondary cracking resulting from an encounter with a

meteoroid that would not have sufficient kinetic energy to penetrate the heat pipe wall.

More work is required to develop the most reliable penetration extrapolation equation so that radiator weights can be kept to a minimum. Also, a clearer definition of the correlation factor, K_0 , needs to be obtained for titanium and its alloys for the same reason. It would also be advisable to attempt to perform hypervelocity impact experiments on titanium at lower particle energies to better simulate the critical standard meteoroid.

ACKNOWLEDGEMENTS

The authors wish to express their appreciation to those individuals at the University of Dayton who made significant contributions to this study: Mark Laber and Chris Williams assisted with the experiments; Andrew Piekutowski assisted in the development of the improved gun seal; and Dr. Lee Cross designed the pulsed-light driver. At Los Alamos we wish to thank Charles Javorsky who performed the optical and scanning electron microscopy.

REFERENCES

1. W. A. Ranken and D. R. Koenig, "Baseline Design of the Thermoelectric Reactor Space Power System," in Proceedings of the 14th Intersociety Energy Conversion Engineering Conference (IECEC), August 5-10, 1979, Boston, MA.
2. G. A. Bennett, "Conceptual Design of Heat Pipe Radiator," Los Alamos Scientific Laboratory Report No. LA-6939-MS (September 1977).
3. B. G. Cour-Palais, "Meteoroid Environment Model-1969 (Near Earth Lunar Surface)," National Aeronautics and Space Administration Report No. NASA-SP-8013 (March 1969).
4. J. W. Gehring, Jr., "Engineering Considerations in Hypervelocity Impact," in High-Velocity Impact Phenomena, R. Kinslow, Ed. (Academic Press, NY, 1970), pp. 463-514.
5. V. C. Frost, "Meteoroid Damage Assessment," National Aeronautics and Space Administration Report No. NASA SP-8042 (May 1970).
6. E. Schneider, "Velocity Dependence of Some Impact Phenomena," presented at ESA Comet Halley Micrometeoroid Hazard Workshop, Nordwick, USSR, April 1979.

7. N. Clough, S. Lieblein, and A. R. McMillan, "Dimple, Spall and Perforation Characteristics of Thin Plates of Nine Materials Under Hypervelocity Impact," National Aeronautics and Space Administration Report No. NASA TN-D-5625 (January 1970).
8. J. H. Diedrich, I. J. Loeffler, and A. R. McMillan, "Hypervelocity Impact Damage Characteristics in Beryllium and Graphite Plates and Tubes," National Aeronautics and Space Administration Report No. NASA-TN-D-3018 (1965).
9. E. P. Bruce, "Hypervelocity Impact of Single Thin Sheet Structures - Incipient Perforation Conditions," in Proceedings of the Seventh Hypervelocity Impact Symposium, Vol. VI, Experiments, Tampa, Florida, Nov. 17-19, 1964 (US Government Report No. AD-463,232), pp. 141-167.
10. R. E. Winter, "Adiabatic Shear of Titanium and Polymethylmethacrylate," *Phil. Mag.* 31, (1975), 765-773.
11. H. C. Rogers, "Adiabatic Plastic Deformation," *Ann. Rev. Mater. Sci.* 9 (1979), 283-311.
12. M. A. Backman and S. A. Finnegan, "The Propagation of Adiabatic Shear," in Metallurgical Effects at High Strain Rates, R. W. Rhode, B. M. Butcher, J. R. Holland, and C. H. Karnes, Eds. (Plenum Press, NY, 1973), 531-543.

Printed in the United States of America
 Available from
 National Technical Information Service
 US Department of Commerce
 5285 Port Royal Road
 Springfield, VA 22161

Microfiche (A01)

NTIS		NTIS		NTIS		NTIS	
Page Range	Price Code						
001-025	A02	151-175	A08	301-325	A14	451-475	A20
026-050	A03	176-200	A09	326-350	A15	476-500	A21
051-075	A04	201-225	A10	351-375	A16	501-525	A22
076-100	A05	226-250	A11	376-400	A17	526-550	A23
101-125	A06	251-275	A12	401-425	A18	551-575	A24
126-150	A07	276-300	A13	426-450	A19	576-600	A25
						601-up*	A99

*Contact NTIS for a price quote.

Los Alamos